Bulletin of Volcanology (2023) 85:2
https://doi.org/10.1007/s00445-022-01621-0

RESEARCH ARTICLE

Pre-eruptive Conditions of the 3 March 2015 Lava Fountain of Villarrica Volcano (Southern Andes)

Jorge E. Romero[1] · Eduardo Morgado[2] · Alessandro Pisello[3] · Felix Boschetty[4] · Maurizio Petrelli[3] · Francisco Cáceres[5] · Mohammad Ayaz Alam[6] · Margherita Polacci[1] · José L. Palma[7] · Fabio Arzilli[8] · Franco Vera[9] · Romina Gutiérrez[10] · Daniele Morgavi[11]

Received: 30 May 2022 / Accepted: 19 November 2022 / Published online: 6 December 2022

Abstract

Villarrica or Rukapillan (35.9°S; 2,847 m a.s.l.) is one of the most active volcanoes in South America and is the highest-risk volcano in Chile. It has an open conduit with a persistent lava lake. On the 3 March 2015, Strombolian activity rapidly progressed into a 1.5-km-high lava fountain, erupting at least ~ 2.4×10^6 m^3 of tephra. Soon after, the activity returned to mild Strombolian "background" explosions, which lasted until early 2017. Understanding the pre-eruptive conditions of such paroxysmal events is fundamental for volcanic hazard assessment. We present major and trace element geochemistry for glass and crystalline phases of basaltic andesite paroxysm pyroclasts (52–56 wt.% SiO_2), and for the subsequent Strombolian "background" activity through February 2017 (54–56 wt.% SiO_2). The lava fountain source magma was initially stored in a deeper and hotter region (9.4–16.3 km; ca. 1140 °C) and was then resident in a shallow ($\leq$0.8 km) storage zone pre-eruption. During storage, crystallising phases comprised plagioclase ($An_{66–86}$), olivine ($Fo_{75–78}$) and augite ($En_{46–47}$). Equilibrium crystallisation occurred during upper-crustal magmatic ascent. During storage in the shallower region, magma reached H_2O saturation, promoting volatile exsolution and over-pressurization, which triggered the eruption. In contrast, subsequent "background" explosions involving basaltic-andesite were sourced from a depth of $\leq$5.3 km (ca. 1110 °C). Pre-eruptive conditions for the 2015 lava fountain contrast with historical twentieth-century eruptions at Villarrica, which were likely driven by magma that underwent a longer period of mixing to feed both effusive and explosive activity. The rapid transition to lava-fountaining activity in 2015 represents a challenging condition in terms of volcano monitoring and eruption forecasting. However, our petrological study of the pyroclastic materials that erupted in 2015 offers significant insights into eruptive processes involving this type of eruption. This aids in deciphering the mechanisms behind sudden eruptions at open conduit systems.

Keywords Basaltic volcanism · Pyroclast · Magma ascent · Fragmentation · Open-vent · Lava lake

Introduction

The textural and compositional study of pyroclastic products is a powerful tool for constraining plumbing system architecture and the physicochemical processes experienced by the magma during ascent prior to eruption. These processes include both pre-eruptive storage, mixing, crystallisation, assimilation and degassing (Corsaro and Miraglia 2005; Blundy and Cashman 2008; Beckett et al. 2014; Morgavi et al. 2017; Cashman and Edmonds 2019; Lerner et al. 2021; Re et al. 2021), as well as syn-eruptive fragmentation styles and mechanisms (e.g., Heiken 1972; Luhr and Carmichael 1990; Dellino et al. 2012; Cioni et al. 2008; Schmith et al. 2017; Ross et al. 2022). Open conduit volcanoes are characterised by their persistent outgassing and mildly explosive activity between major eruptions (Edmonds et al. 2022 and references therein). At mafic open conduit systems, eruptive activity is characterised by periods of degassing or small eruptions intercalated with

Editorial responsibility: U. Kueppers

This paper constitutes part of a topical collection:

What pyroclasts can tell us

✉ Jorge E. Romero
jorge.romero@postgrad.manchester.ac.uk

Extended author information available on the last page of the article

more energetic, sometimes sudden, paroxysmal events (e.g., Lyons et al. 2010; Bertagnini et al. 2011; Rose et al. 2013; Pioli et al. 2014; Spina et al. 2019; Giordano and De Astis 2021; Métrich et al. 2021; Viccaro et al. 2021). These paroxysmal events pose an immediate treat for the communities living in the proximal areas (Andronico et al. 2021; Giordano and De Astis 2021); exposed populations may underestimate the scale of potential hazards these volcanoes can generate, especially when low-level activity appears to be dominant (Rose et al. 2013). Additionally, rapid changes in the magma column level or lateral magma drainage may represent an additional threat for communities living near these volcanoes (e.g., Witham et al. 2006; Valade et al. 2016; Patrick et al. 2019; Shreve et al. 2019; Romero et al. 2022). The pyroclastic products related to paroxysmal events in open conduit systems may provide important clues to understanding their behaviour and related hazards (e.g., Pioli et al. 2014; Métrich et al. 2021; Viccaro et al. 2021; Zuccarello et al. 2021).

Villarrica (or Rukapillan in the Mapuche language) is an active composite volcano in the Southern Andes of Chile. It is classified as the highest-risk volcano in Chile (SERNAGEOMIN 2020), with a death toll of ca. 100 during the twentieth century, and > 100 eruptions documented between AD 1384 and AD 1971 (Naranjo and Moreno 2004; Van Daele et al. 2014). Since its 1984 eruption, Villarrica has exhibited open conduit behaviour with the presence of magma at a high level within its conduit, sometimes exposed as a lava lake, and producing continuous outgassing, short-lived lava fountains and Strombolian explosions (Palma et al. 2008). On the 3 March 2015, Strombolian activity became increasingly vigorous and within 30 min culminated in a short-lasting (ca. 16 min) 1.5 km-high lava fountain accompanied by an eruptive column reaching 10.8 km above the main crater (Romero et al. 2018). The crater perimeter was completely covered by agglutinated products with a thickness of a few meters, while the interaction of incandescent materials with the ice-covered that flanks of the volcano triggered lahars that flow down four radial rivers (Edwards et al. 2018). Despite producing no fatalities, this eruption displayed a distinct behaviour compared to other historical eruptions, which mainly produced long-lasting Strombolian activity, lava effusion and lava fountaining (e.g., Petit-Breuilh and Lobato 1994; Moreno and Clavero 2006; Castruccio and Contreras 2016; Pizarro et al. 2019). Thus, understanding the pre-eruptive conditions of the 2015 eruption is key to a better assessment of Villarrica's volcanic hazards and regime change at open vent systems.

In this paper, we present the first comprehensive petrological and geochemical investigation of the pyroclastic products of the 3 March 2015 eruption, as well as pyroclasts produced by mild Strombolian activity following the fountaining event in December 2015 and February 2017. This work contains compositional analyses and thermobarometric estimates for the March 2015 lava fountain of Villarrica. These results are used to understand the processes leading to the lava fountain, which are compared to similar changes in eruptive regime at other open conduit systems.

Geological and Volcanological Background

Villarrica (2847 m. a.s.l.; 39°25′S, 71°56′W; Fig. 1a) has been active since the Middle Pleistocene (Moreno and Clavero 2006). Construction of an ancient Pleistocene basaltic-to-dacitic edifice culminated in the formation of a 7 × 4-km-diameter caldera ca. 95 ka (Moreno and Clavero 2006). Subsequent activity was dominated by explosive eruptions, such as the 10 km^3 (non-DRE) Licán mafic ignimbrite dated at ca. 13.9 ka (Moreno and Clavero 2006; Lohmar et al. 2012). Amongst Villarrica's Holocene effusive and pyroclastic deposits, Villarrica also sourced the basaltic-andesite Pucón Ignimbrite (~ 4.8 km^3) ca. 3.7 ka (e.g., Moreno and Clavero 2006; Silva Parejas et al. 2010; Moreno and Toloza 2015). Late-Holocene explosive activity includes the Chaimilla tephra fallout deposit, which was erupted at ca. 3.2 ka and with a total non-DRE volume of ~ 0.6 km^3 (Costantini et al. 2011; Pioli et al. 2015).

Villarrica's eruptions of October 1948 and February 1949 (VEI ~ 3) were characterised by lava fountains of several hundred meters in height, with eruption columns up to 8 km high and simultaneous lava effusion to build lava flow fields with a volume of $16 \pm 4 \times 10^6$ m^3 (Moreno and Clavero 2006; Pizarro et al. 2019). On the 2nd of March 1964, a 600-m-high lava fountain triggered a series of lahars affecting the village of Coñaripe and killing ca. 22. Also, on 29 October 1971, a 2-km-long fissure fed lava fountains reaching 600 m in height and two lava flows totalling ~ 50×10^6 m^3, producing destructive lahars due to ice-melt (Castruccio and Contreras 2016).

Volcanic Activity Between March 2015 and February 2017

The 3 March 2015 lava fountain was preceded by volcanic unrest starting in August 2014 (Romero et al. 2018). Signs of this unrest included increased long-period (LP) seismicity, higher SO_2 fluxes and CO_2/SO_2 ratios, thermal anomalies and a sharp increase in the radiated infrasound and Strombolian activity (e.g., Johnson and Palma 2015; Aiuppa et al. 2017; Delgado et al. 2017; Johnson et al. 2018; Romero et al. 2018; Palma et al. 2008).

The paroxysmal phase began at 03:10 am (all times are local, UTC − 04:00 in wintertime and UTC − 03:00 in summertime) and ended around 03:26 am, producing a fallout deposit (Fig. 1a) found up to 100 km SE of Villarrica and

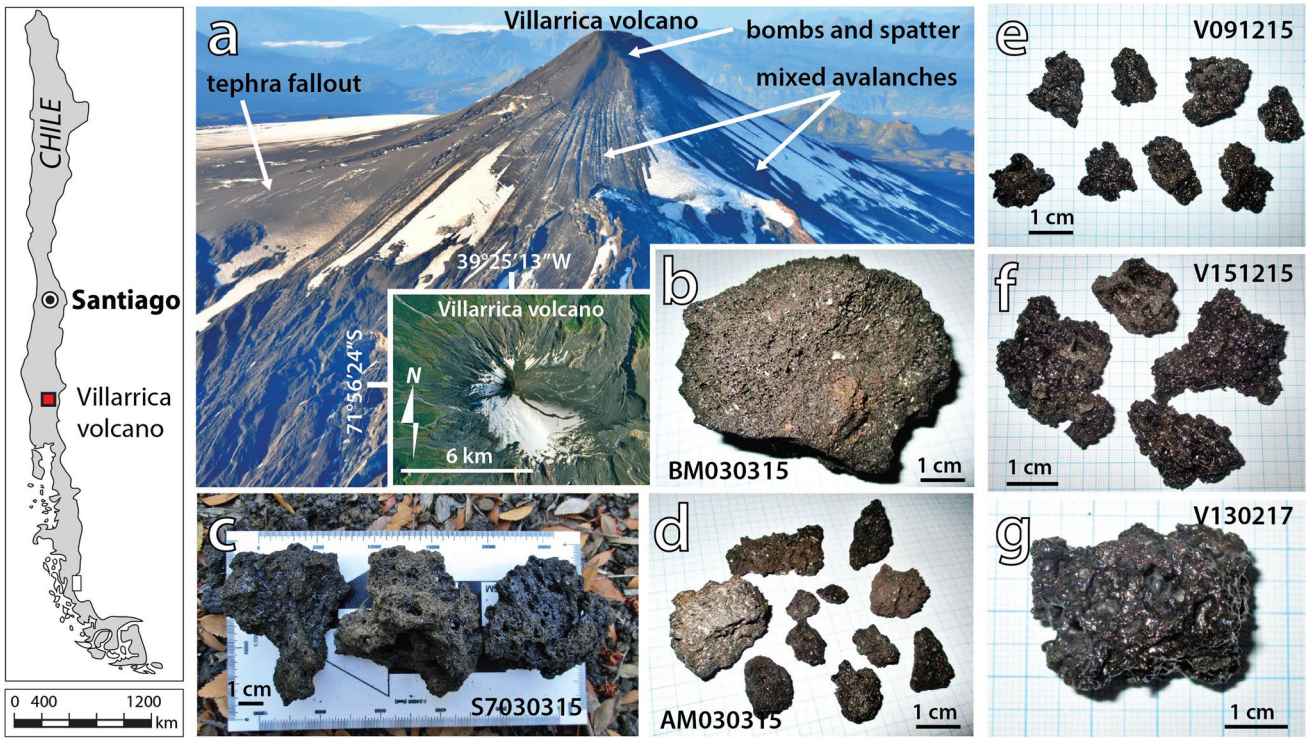

Fig. 1 Volcanic products of the 2015–2017 eruptive activity. **a** Aerial view of the 3 March 2015 deposits seen from the northwest (courtesy of Daniel Basualto). Samples analysed in this study: **b** ballistic bomb, **c** lapilli, **d** mixed avalanche blocks, **e** 9th of December 2015 lapilli, **f** 15th of December 2015 lapilli and **g** 13th of February 2017 lapilli

comprising 1.4×10^9 kg of basaltic-andesite tephra (Romero et al. 2018). Close to the vent (< 3 km), radially distributed eruptive products consisted of spatter, ballistic bombs, clastogenic lavas and mixed avalanche deposits (Fig. 1a; SERNAGEOMIN 2015; Romero et al. 2018; Edwards et al. 2018). The avalanches were of pyroclasts mixed with snow and/or ice, also called ice-slurries (Breard et al. 2020).

Subsequent activities in December 2015 and February 2017 were classified as within the background for the typical activity of the volcano (SERNAGEOMIN 2015, 2017). During December 2015, the lava lake remained visible < 150 m below the crater rim, exhibiting incandescence at night and mild Strombolian explosions, some of which reached the crater rim. SERNAGEOMIN (2015) reported 5788 LP and six volcano-tectonic (VT) earthquakes during this period, and on 15 December, Strombolian activity produced a 200-m-high ash column. This was followed by a 146 MW thermal anomaly detected by MIROVA (Coppola et al. 2020) on 16 December plus degassing of ~ 2800 ± 1100 tons of SO_2 on the 22 December (SERNAGEOMIN 2015). In January 2016, Moussallam et al. (2016) described a lava lake at a depth of 140 m, with fresh spatter on the crater walls a few 10 s of meters above the lava surface and SO_2 emissions of 160 t/day on average. According to available photographic evidence, during February 2017, the lava lake was higher within the crater, likely < 100 m below the crater rim, with a spatter roof concealing most of its surface and explosions releasing pyroclasts through a narrow opening in the roof, similar to the activity observed at the end of 2004 (Palma et al. 2008). Over the same period, SERNAGEOMIN (2017) reported 2466 LP and 13 VT earthquakes; a thermal anomaly was detected by MIROVA on the 10th of February reaching 9 MW (Coppola et al. 2020) and monthly SO_2 degassing averaged 259 ± 45 t/day.

Methods

Sampling

We analysed six juvenile samples (Table 1). Three correspond to the 3 March 2015 eruption products, including a ca. 10 cm-diameter bomb found in the vicinity of the crater (BM030315; Fig. 1b), coarse lapilli (up to 4–6 cm in diameter) from the tephra fallout deposit (S7030315; Fig. 1c), and fragments of a dense block transported by mixed avalanches (AM030315; Fig. 1d). These samples were picked from bulk pyroclastic deposits, and they are representative of the most abundant juvenile particles of these deposits. Juvenile bombs are homogeneous in texture, and they were found as either

loose or agglutinated pyroclasts. We sampled the loose bomb from the upper part of the bomb-and-spatter deposit (Fig. 1b). Despite the external textural differences, lapilli particles were texturally homogeneous with low crystal contents and glassy groundmasses (e.g., Fig. 1c; Romero et al. 2018). In contrast, the mixed avalanche deposits exhibited a large variety of particle shapes and crystallinities (Fig. 5d; cf. Edwards et al. 2018), probably related to different cooling histories resulting from variable degrees of interaction with the snowpack (Edwards et al. 2018). We sampled fragments from a low vesicularity (< 1% vol.) juvenile block lying in the mixed avalanche. The final three samples correspond to medium-to-coarse lapilli (2–5 cm diameter) deposited on the snowpack surrounding the crater rim during subsequent activity. These pyroclasts were collected after mild-Strombolian explosions on the 9th and 15 December 2015 (V091215 and V151215; Fig. 1e, f) and on the 13 February 2017 (V130217; Fig. 1g).

The same samples here reported were analysed in the work of Romero et al. (2018) for petrography, density and semi-quantitative X-ray fluorescence using electron dispersive spectroscopy. We here extend the analysis for detailed petrology and the study of pre-eruptive conditions as described onwards.

Analytical Techniques

All six samples were mounted in epoxy resin, and the epoxy blocks were dried for 12 h under a vacuum at the Department of Physics and Geology, University of Perugia (Italy). They were then cut and polished to form resin chips with surface areas of between 10 and 15 mm^2 to produce a surface suitable for microanalysis. All analysed surfaces correspond to the interiors of the pyroclasts. Major element compositions of groundmass and major silicate mineral phases (plagioclase, Pl; clinopyroxene, Cpx; and olivine, Ol) and backscattered electron (BSE) images were obtained using a Cameca SX100 electron probe microanalyser (EPMA) at the Department of Earth and Environmental Sciences at the Ludwig-Maximilians University of Munich (Germany). The operating conditions were a 15 kV acceleration voltage, 20 nA beam current, a defocused 10 µm beam for glass analysis and 1 µm beam for mineral phases. The instrument was calibrated using the following internal standards: orthoclase for Al and K, albite for Si and Na, wollastonite for Ca, periclase for Mg, ilmenite for Ti, iron oxide for Fe and chromium oxide for Cr. The uncertainty is between 1 and 5% for major elements and up to 10% for elements at concentration < 0.2 wt.% when comparing the known compositions of standards with the measurements of the same standards.

EPMA spots (57) were selected for subsequent trace-element compositional analysis of matrix glasses and minerals. We performed laser-ablation inductively-coupled-plasma

Table 1 Summary of sample textural information, values are abundance in modal percent. Ol olivine, Plg plagioclase, Cpx clinopyroxene, —not present

Sample	Date	Type	Phenocrysts			Groundmass				Texture and vesicle shape/interconnection
			Ol	Pl	Cpx	Ol	Pl	Cpx	Glass	Vesicles	
S7030315	03/03/15	Scoria	2	16	< 1	-	< 1	-	23	59	Vitrophyric, glomeroporphyritic and seriate. Subrounded to irregular vesicles, low interconnection
AM030315	03/03/15	Mix. av	12	31	< 1	1	13	2	40	1	Porphyritic, glomeroporphyritic and seriate. Disconnected small vesicles
BM030315	03/03/15	Bomb	< 1	8		11	22	5	6	48	Porphyritic, seriate. Irregular vesicles, moderate interconnection
V091215	09/12/15	Scoria	2	18	< 1	-	-	-	34	52	Vitrophyric. Small subrounded to irregular vesicles, moderate interconnection
V151215	15/12/15	Scoria	6	53	< 1	-	-	-	15	26	Vitrophyric and glomeroporphyritic. Small subrounded to irregular vesicles, moderate-to-high interconnection
V130217	13/02/17	Scoria	-	24	-	-	1	-	25	50	Vitrophyric and glomeroporphyritic. Small subrounded vesicles, low interconnection

mass-spectrometry (LA-ICP-MS) using a Teledyne Photon Machine G2 laser ablation system coupled to a Thermo Fisher Scientific iCAP-Q ICP-MS housed at the Department of Physics and Geology, University of Perugia. The operative laser conditions were circular laser spots of 15 and 25 μm in diameter, a laser fluence of 3.5 Jcm^{-2}, and a repetition rate of 10 Hz. The background was acquired for 25 s, followed by 40 s of ablation, and 25 s of washout. Helium was used as the carrier gas, with Ar and N_2 used as makeup gases to avoid plasma destabilisation and to enhance sensitivity, respectively. NIST SRM 610 and USGS BCR2G standards were used as calibrators and quality control, respectively, following the approach described in Viccaro et al. (2021). The ^{29}Si, previously analysed by EPMA, was the internal standard. Under the investigated operating conditions, precision and accuracy are typically better than 10%.

The main petrographic features (proportions of phenocrysts, glass, and vesicles) of all the collected products were quantified by image processing techniques via the "Background Extraction" of pseudo-coloured BSE images using the freeware JMicrovision (Roduit 2008). For each sample, we used between 3–4 images; the individual proportions were averaged and the standard error on the estimates was 4.5%.

Estimating Pre-eruptive Conditions

Successful mineral-liquid thermobarometry requires chemical equilibrium between pairs of mineral phases and liquid (liq). We used plagioclase, olivine and clinopyroxene in the same proportions as those obtained from our petrological analysis (Table 1). The liquid composition was obtained from the glass chemistry of each sample and a bulk-rock composition reported by McGee et al. (2017). Cations per formula unit (cfu) for all liquid components were calculated as anhydrous cation fractions, as in Putirka (2008). The $Fe^{3+}/Fe\sum$ ratio of the liquid was calculated by assuming an oxygen fugacity at the Quartz-Fayalite-Magnetite (QFM) buffer, as in Lohmar et al. (2012), using the method of Kress and Carmichael (1991). Pl-liq, and Ol-liq equilibria were tested using K_D^{An-Ab} (Pl-liq) = 0.27 ± 0.11 (Putirka 2008) and K_D^{Fe-Mg} (Ol-liq) = 0.3 ± 0.03 (Roeder and Emslie 1970; Supplementary Material 1). Cpx-liq equilibrium was tested using the four criteria of Neave and Putirka (2017) with K_D^{Fe-Mg} (Cpx-liq) = 0.28 ± 0.03. Cpx-liquid pairs were filtered to be within the 10% of Fe–Mg, DiHd component, CaTs component and Ti-contents (Neave and Putirka 2017 and references therein; Supplementary Material 1). Clinopyroxene cfu was calculated on a 6-oxygen basis, those with total cfu outside the range 4.0 ± 0.02 were discarded and the method of Droop (1987) was used to calculate the ratio of Fe^{2+} to Fe^{3+}. All glass compositions can be found in Supplementary Material 2.

We used multiple thermobarometers and hygrometers to calculate magmatic-intensive variables (T = temperature, P = pressure and H_2O). The results of these can be found in Table 2. Water contents were calculated using a Pl-liq equilibrium hygrometer (Waters and Lange 2015). Chemical compositions of the melt phase and the rims of plagioclase crystals obtained from EPMA analyses were used as input values, as well as the initial temperature and pressure of the magma, determined using a pyroxene-liquid method (Eq. 33 for T and Eq. 30 for P in Putirka 2008). Ol-liq thermometers from Beattie (1993), Eq. 22 of Putirka (2008), and Sisson and Grove (1993) were compared. The thermometer of Beattie (1993) is the best constrained of the three for anhydrous melts, but not calibrated for hydrous melts (Putirka 2008), so the Putirka (2008) and Sisson and Grove (1993) thermometers were used for comparison. All three thermometers are pressure-dependent; hence we selected a pressure of 1 kbar to estimate the temperatures. This is based on the deformation source detected by Delgado et al. (2017) after the March 2015 eruption and is equivalent to a depth of 4.2 km (using a crustal density of 2700 kg/m^3). This depth is also consistent with the location of a shallow reservoir reported in the literature for Villarrica (Lohmar et al. 2012; Morgado et al. 2015; Pizarro et al. 2019; Boschetty et al. 2022).

Results

Textures

The 2015 juvenile samples show vitrophyric, porphyritic and seriate textures (Fig. 2a; Table 1) with a mineral assemblage consisting of Pl, Ol and very scarce Cpx phenocrysts. Crystals were classified as phenocrysts (> 300 μm), microphenocrysts (30–300 μm) and microlites (< 30 μm) following Zellmer (2021). In contrast to the 2015 samples, the 13th of February 2017 lapilli exclusively contain Pl phenocrysts and microlites (Table 1). In the 2015 lava fountain, mixed avalanche and bomb samples plagioclase crystals (whole size range) are predominantly rectangular prisms. While in the rest of the samples, plagioclase displays an acicular habit. All plagioclase phenocrysts are subhedral to euhedral, and in some cases, they exhibit normal or oscillatory zoning. Subhedral to euhedral sieve-textured Pl phenocrysts (800–1300 μm) are only present in the 3 March 2015 products (Fig. 2b). Ol phenocrysts are anhedral to euhedral, 100–800 μm in length, and show normal concentric zoning. In the 2015 samples, individuals or groups of anhedral Ol are frequently found next to, or enclosed by, larger Pl phenocrysts. Cpx phenocrysts have euhedral blocky shape and vary from 60 to 400 μm in size (Fig. 2a). Except for the mixed avalanche sample, all other samples display a glassy groundmass,

Table 2 Magmatic intensive variables estimated using thermobarometry and hygrometry via multiple methods. For mineral-liquid methods, the arithmetic mean of all equilibrium minerals per sample is given and one standard deviation is shown in brackets. For two reported values the upper corresponds to core and the lower to rims. Sample AM030315* did provide minerals in equilibrium with bulk rock composition reported in McGee et al. (2017), whereas all the rest are compared to their corresponding average glass compositions reported in Supporting Table 1

Technique (unit)	Method	S7030315	AM030315*	BM030315	V091215	V151215	V130217
Ol-liq T (°C)	Beattie (1993)	1146	1154	1154	1133	1138	n.p
Ol-liq T (°C)	Sisson and Grove (1993)	1091 (4.3) 1089 (6.0)	1090 (3.0) 1090 (1.5)	1092 (2.3) 1096 (5.6)	1074 (1.0)-	1077.3 (1.1) 1077 (0.7)	n.p. n.p
Ol-liq T (°C)	Putirka (2008) Eq. 22	1135 (5.3) 1135 (7.0)	1136 (3.6) 1135 (1.9)	1138 (2.8) 1144 (7.0)	1112 (1.0)	1117 (1.3) 1116 (0.8)	n.p
Ol-liq H (wt% H_2O)	Gavrilenko et al. (2016)	4.0 (0.4)		2.2 (2.0)	4.4 (0.5)	-	n.p
Pl-liq T (°C)	Putirka (2008) Eq. 24a	1111 (3.4) 1114 (4.2)	1140 (5.3) 1136 (2.4)	1105 (2.4)-	1115 (3.1) 1112 (4.4)	1114 (2.4) 1112 (1.0)	1111 (6.2) 1110 (0.1)
Pl Saturation T (°C)	Putirka (2008) Eq. 26	1118 (2.1) 1125	1143 (2.4) 1143 (2.5)	1115-	1122 1122	1122 1122	1118 1118
Pl-liq B (kbar)	Putirka (2008) Eq. 25a	0.2 (0.3) 1.2 (0.6)	3.5 (0.7) 4.0 (0.2)	1.0 (0.3)-	0.3 (0.3) 0.5 (0.5)	0.3 (0.3) 0.6 (0.1)	0.4 (0.2) 0.1
Pl-liq H (wt% H_2O)	Putirka (2005) eqn. H	1.5 (0.1) 1.7 (0.2)	1.9 (0.4) 2.1 (0.1)	1.6 (0.1)-	1.7 (0.2) 0.8 (0.2)	1.6 (0.1) 1.7 (0.1)	1.6 (0.1) 1.4
Pl-liq H (wt% H_2O)	Waters and Lange (2015)	1.3–1.4		0.7	0.9–1.0	1.0	0.9–1.1
Cpx-liq T + B (°C/kbar)	Putirka (2008) Eq. 33 + Putirka (2008) Eq. 30	-		n.p	n.p	1150/3.8	n.p
Cpx-liq T + B (°C/kbar)	Putirka (2008) Eq. 33 + Neave and Putirka (2017)	1143/2.8		n.p	n.p		n.p

Ol olivine, *Plg* plagioclase, *Cpx* clinopyroxene, *T* thermometry, *B* barometry, *H* hygrometry, *eqn.* equation,—no equilibrium pairs, *n.p.* mineral not present in sample

made up of Pl (< 22%), Ol (< 11%), Cpx (< 5%) and Fe-Ti oxides (< 1%), which are occasionally arranged in a hyalopilitic or intergranular fashion (Fig. 2c). Occasionally, Pl microphenocrysts are arranged in glomeroporphyritic clots (present in all the samples). Pl microlites (10–30 µm) are acicular euhedral to subhedral, while Ol microlites are euhedral (< 20 µm), and generally arranged in glomeroporphyritic clusters. All Cpx microlites are anhedral and their size is always < 10 µm.

The 3 March 2015 samples display a wide range of vesicle fractions and crystallinities. The lapilli sample has ~ 59% sub-spherical vesicles with incipient coalescence and contains 16% Pl, 2% Ol and < 1% Cpx phenocrysts, while glass represents 23% (Fig. 2d). Pl microlites are scarce (< 1%). The 2015 bomb is also highly vesicular (48%), whereas vesicles are irregular, developing increasing coalescence, and the sample contains 8% Pl, 1% Ol and 44% groundmass (Fig. 2e; 22% microlites of Pl, 11% Ol, 5% Cpx and 6% glass). The highest-crystallinity sample corresponds to the mixed avalanche block, with 31% Pl, 12% Ol, < 15% Cpx and 15% microlites (Fig. 2f; 13% Pl, 1% Ol and 1% Cpx). Despite its higher crystallinity, glass represents 40% in the mixed avalanche and only 1% of vesicles with irregular shapes and lack of coalescence are found.

All post-lava fountain samples also share a very low proportion of microlites (0.1–0.9%), high vesicularity and glassy groundmass. The December 2015 samples display variable vesicularities (Fig. 2g, h; 26–53%) and contain 18–53% Pl, 2–6% Ol and 15–34% glass. Cpx phenocryst are always < 1%. Finally, the February 2017 sample consists of only plagioclase phenocrysts (38%), 27% low-coalescing sub-spherical vesicles and groundmass glass (Fig. 2i).

Major Elements

Melt Composition

The composition of the groundmass glass in all samples is basaltic andesite (Fig. 3a; 52.1–56.2 wt.% SiO_2). FeO/MgO and Al_2O_3/CaO ratios increase with increasing SiO_2 content (Fig. 3b–c). Trends of increasing Al_2O_3 and CaO, decreasing TiO_2 and FeO, with increasing MgO are also

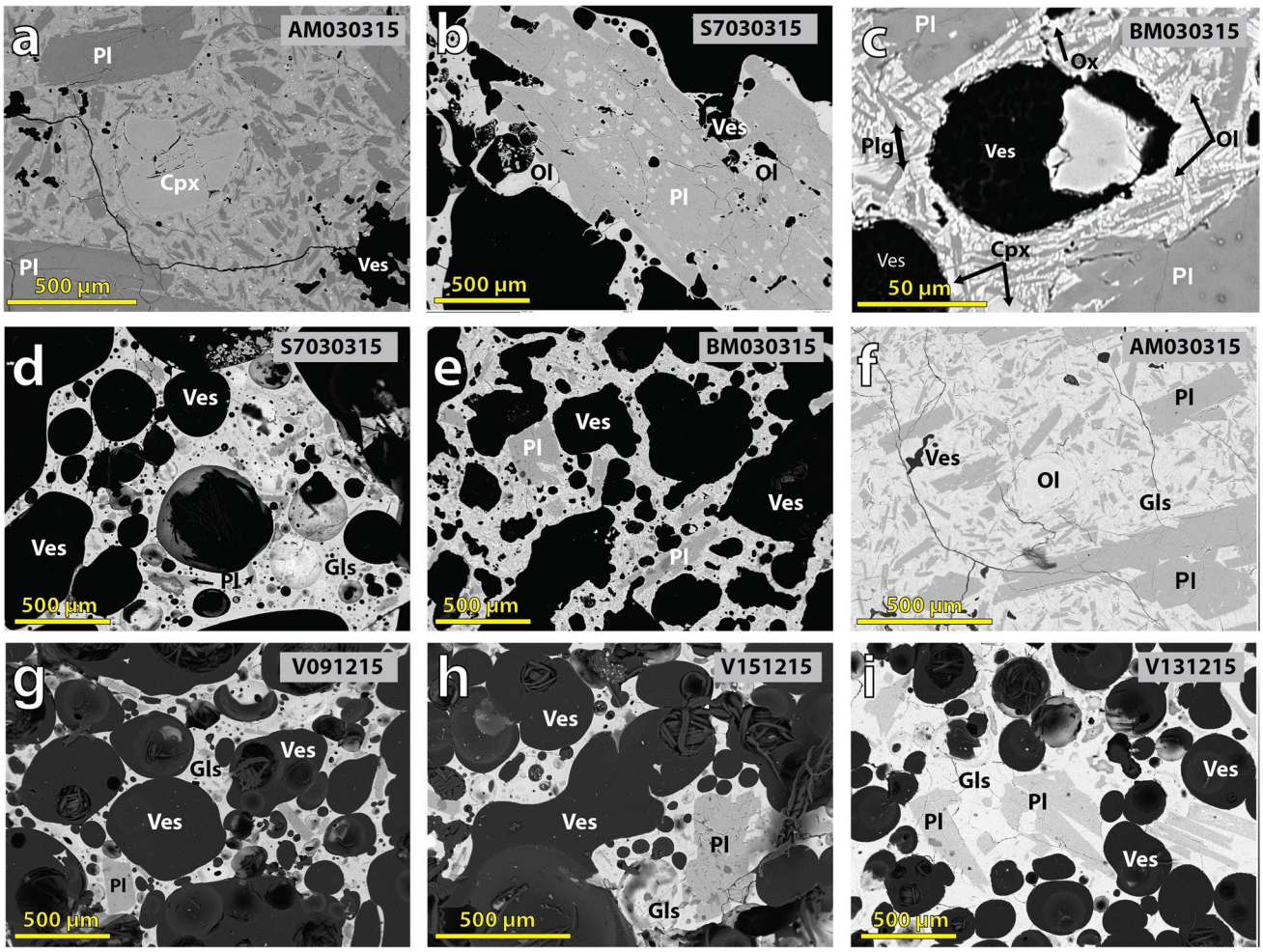

Fig. 2 Backscattered secondary electron images (BSE) of the textural features seen in scoria samples of Villarrica 2015–2017 eruptive activity. **a** Porphyritic and seriate texture and **b** sieve Pl phenocryst, both in the AM0303015 and S7030315 samples, respectively. **c** Detail of the BM030315 sample groundmass, showing Pl, Ol, Px and Ox microlithes. **d** Sub-spherical vesicles and glassy groundmass in S7030315. **e** Irregular vesicles in BM031515. **f** Low-vesicularity and high-crystallinity in the AM030315 sample. **g**, **h** and **i** sub-spherical and highly glassy groundmass in V091215, V151215, and V131215, respectively

observed (Fig. 3d–g). Other oxides, such as MnO, do not vary systematically with SiO_2 (Fig. 3h). The 3 March 2015 samples show the widest compositional range of all the samples. Amongst these, the mixed avalanche sample shows the highest variability. However, most of the Harker plots show silica enrichment (Fig. 3a) and a decrease in FeO/MgO vs. SiO_2 (Fig. 3b). The least evolved composition is primarily represented by the coarse lapilli and the bomb samples. Both samples occupy similar compositional fields when compared to the December 2015 and February 2017 medium-to-coarse lapilli (Fig. 3a; 53.4–55.7 wt.% SiO_2). Most of the 2015 samples span a wider and slightly more evolved compositional field than the past eruptive products (1971–2004), and bulk-rock compositions of historical eruptions (1921–1971; Fig. 1).

Mineral Compositions

We analysed 71 plagioclase, 44 olivine and 5 clinopyroxene phenocrysts (Supplementary Material 2) using which their compositions (Fig. 4a–c), textures (Fig. 4d–f) and zoning (Fig. 4g) can be described. The anorthite (An) contents

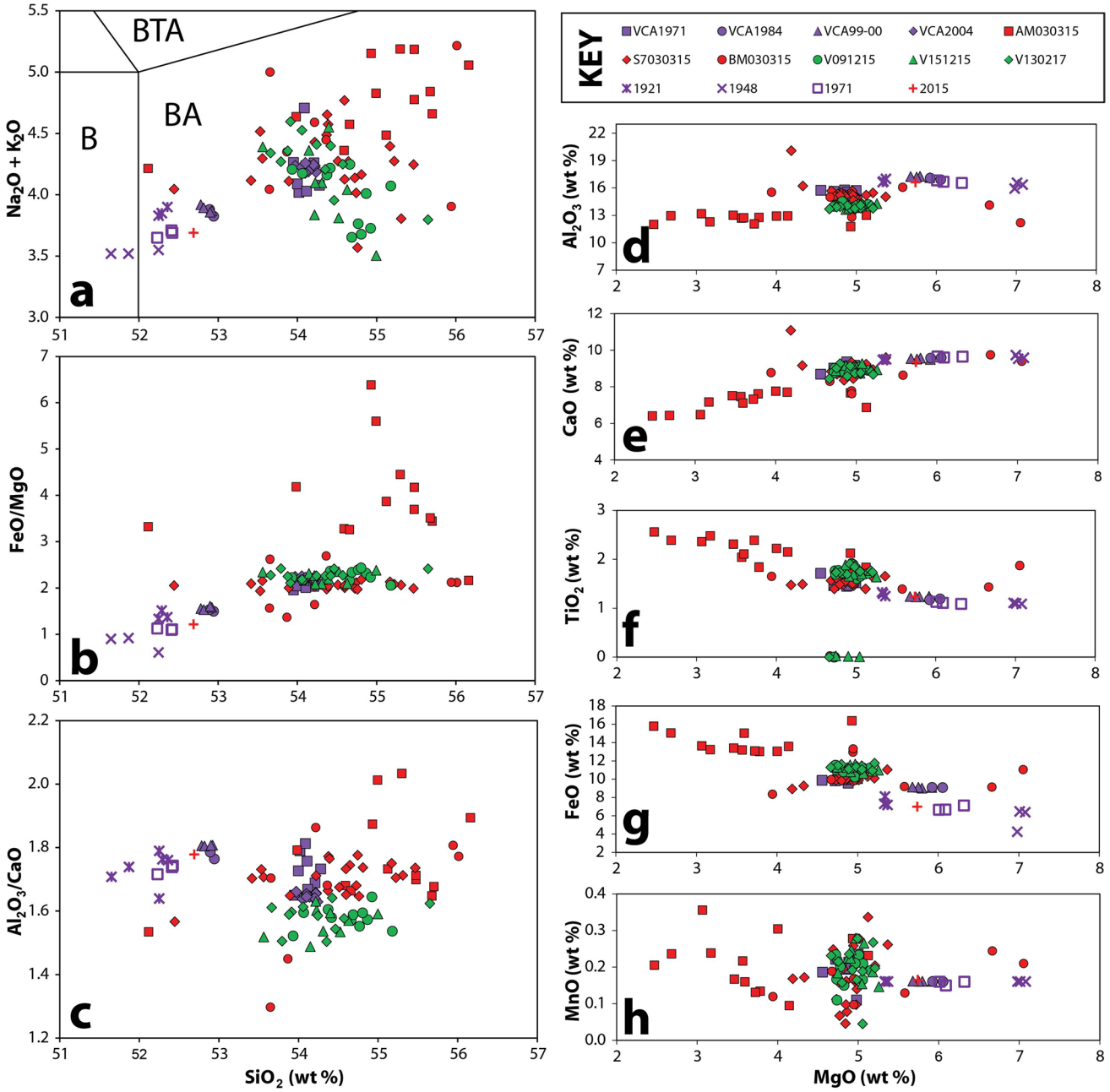

Fig. 3 Normalised, volatile-free glass and bulk-rock geochemistry of the 2015 (red symbols) and 2017 (green symbols) eruptive products of Villarrica compared to products from historical eruptions and the background mild-Strombolian activity between 1999 and 2004 (Witter et al. 2004; Gurioli et al. 2008). Filled symbols are glass compositions and open symbols are bulk rock compositions (Pizarro et al. 2019; McGee et al. 2017). The 2015 bulk-rock composition of McGee et al. 2017 is symbolised with a red cross. **a** Total alkali-silica classification diagram. B basalt, BA basaltic andesite and BTA basaltic trachyandesite. SiO_2 versus **b** FeO/MgO and **c** Al_2O_3/CaO; Plots of MgO v/s **d** Al_2O_3, **e** CaO, **f** TiO_2; **g** FeOt and **h** MnO

($X_{An} = 100 \times Ca/[Na + Ca + K]$ in mols) of the mixed avalanche and the coarse lapilli sample display a relatively wide range of values ($An_{66–86}$). However, most of the crystals are normally distributed around $An_{\sim 70–75}$, especially those of the post-2015 paroxysm samples (Fig. 4a). The 3 March 2015 Pl phenocrysts commonly present normal zoning, with $An_{76–78}$ cores and intermediate regions, and $An_{73–74}$ rims (Fig. 4d, g). Sieve-textured Pl in the mixed avalanche fragments show normal zoning with cores up to $An_{\sim 86}$ and rims nearly $An_{\sim 70}$(Fig. 4d, g).

Forsterite contents ($Fo = 100 \times Mg/[Mg + Fe^{2+}]$ in mols) are broadly similar in most of the olivine phenocrysts.

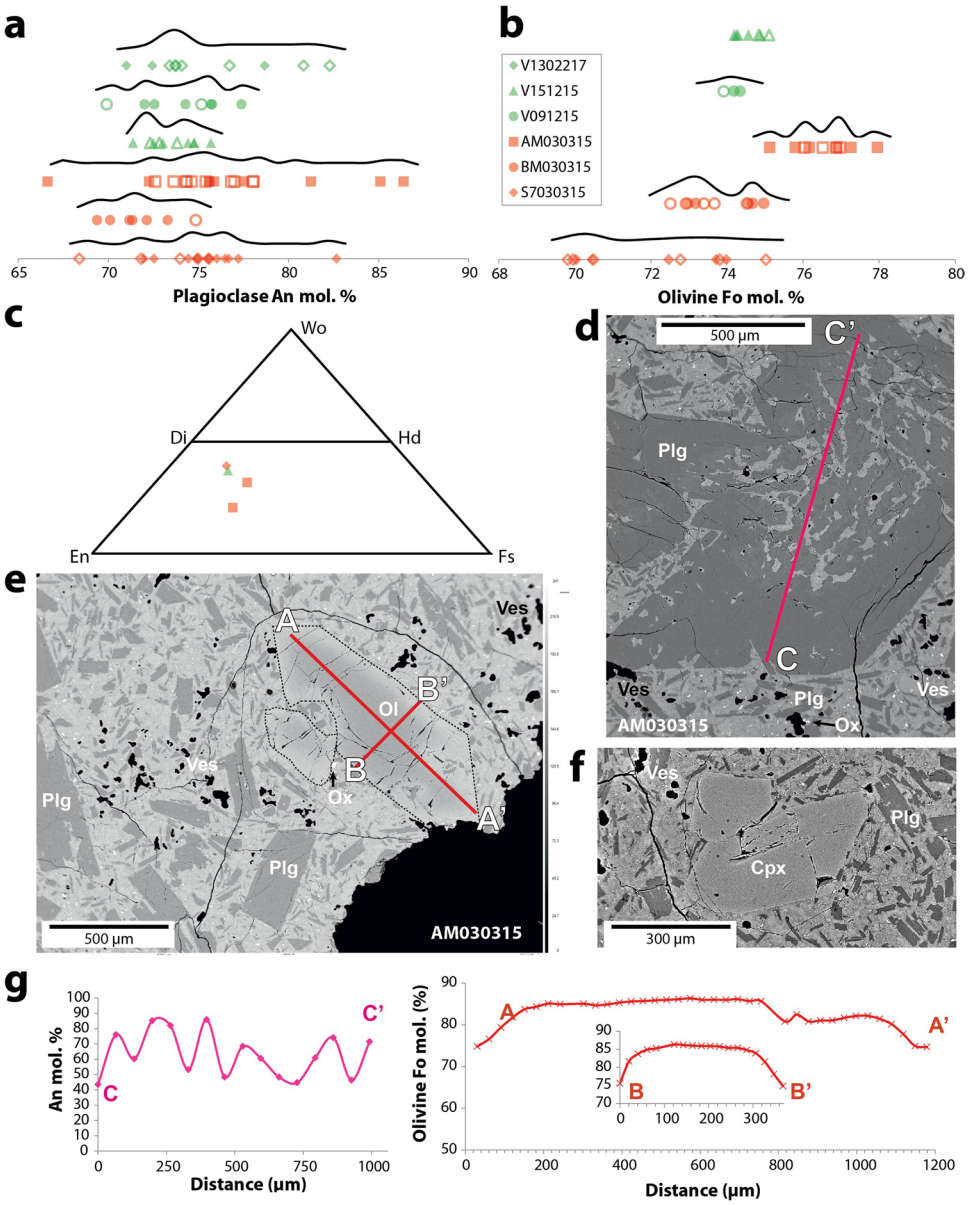

Fig. 4 Plagioclase and olivine phenocryst composition. Filled symbols represent core compositions, while open symbols are used for either rim or core-rim intermediate compositions. **a** Anorthite contents in plagioclase crystals of the 2015–2017 products. **b** Forsterite contents in olivine crystals. **c** Pyroxene classification ternary diagram with the few selected clinopyroxenes in this work. **d**, **e** and **f** show BSE images of plagioclase, olivine, and pyroxene crystals, respectively. Electron microprobe chemical transects (**g**) across sieve plagioclase crystal and olivine from rim to rim, same shown in insets (**d**) and (**e**), respectively

The mixed avalanche sample displays the widest range ($Fo_{75–78}$), with a few cores of the largest Ol phenocrysts reaching Fo_{85} (Fig. 4g), while lower Fo contents are observed in the bomb ($Fo_{72–75}$) and the coarse lapilli ($Fo_{70–75}$) from the 3 March lava fountain (Fig. 4b). The December 2015 olivine displays a much narrower compositional range ($Fo_{74–75}$), and no Ol is present in the February 2017 sample. Similarly, the largest Ol phenocrysts (> 350 µm) display normal zoning and their cores reach $Fo_{\sim 85}$, whereas the rims have $Fo_{\sim 75}$ (Fig. 4e, g). We did not identify any reverse zoning in these crystals.

Cpx is scarce in the samples analysed and only apparent in the 2015 samples. Of the five analyses, only two have Cfu totals of 4.00 ± 0.02; they have a similar augitic composition with $En_{46–47}$, $Wo_{37–38}$ and $Fs_{14–15}$ (Fig. 4c). The five Cpx phenocrysts do not appear to be zoned. The scarcity of Cpx crystals (Fig. 4f) prevents detailed analyses of zoning.

Trace Elements

Melt Composition

Trace-element patterns in glass normalised to primitive mantle (McDonough et al. 1992) (Fig. 5a) show a depletion in both Nb and Ta. Due to its glassy texture, the lava fountain coarse lapilli sample was selected to analyse its trace element pattern, which is similar compared to that of post-lava fountain samples. However, it is slightly more depleted in elements Nb, Ta, La, Ce and those from Pr to Lu (Fig. 5a).

Trace elements from bulk basaltic to basaltic-andesite Holocene-to-historical Villarrica samples reported by Hickey-Vargas et al. (1989) also display a very similar pattern to the 2015–2017 glass. These show overall depletion of all elements, except Sr (Fig. 5a). The same behaviour is observed in REE elements (Fig. 5b). The post-lava fountain samples are also slightly enriched in metals compared to the lava fountain lapilli (Fig. 5c). Despite similarities, the bulk rock compositions of older products show some enrichment in Cr and Ni compared to the 2015–2017 glasses (Fig. 5c).

Mineral Compositions

Chemical rim-to-rim transects within olivine crystals show enrichment of Li towards the rim, with core contents ($Fo_{\sim 85}$) around 1.3 ppm and rims reaching 6.3 ppm (Fig. 5d). We also observed enrichment of Ni towards the core (from 650

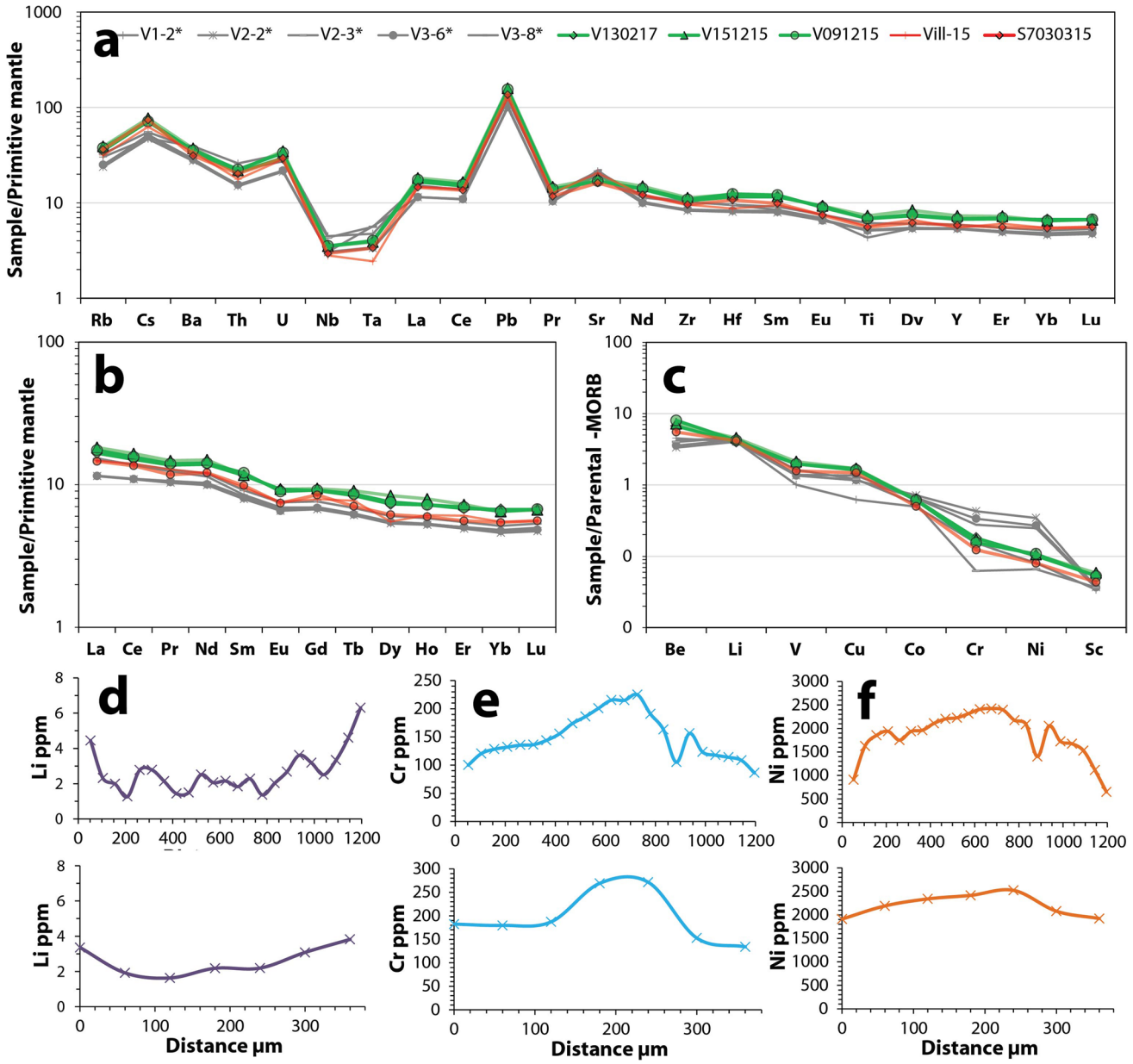

Fig. 5 Trace elements plots for glass compositions of the 2015–2017 samples. **a** Primitive mantle-normalised (Sun and McDonough 1989) spider diagram. **b** Normalised REE abundances. **c** Normalised metals (Parental MORB from Jenner 2017). Bulk-rock compositions for Vill–15 spatter (McGee et al. 2017) and for the historical lavas of Villarrica (Hickey-Vargas et al. 1989) are incorporated in a) to (**c**). Concentrations of (**d**) Li, (**e**) Cr and (**f**) Ni (ppm) in length (upper) and width (lower) transects of an Ol phenocryst with normal zoning (rims to Fo ~ 75 and cores to Fo ~ 85) in AM030315

in the rim to 2400 ppm in the core; Fig. 5e) and Cr (from 70 ppm in the rim to 270 ppm in the core; Fig. 5f). All mineral composition data are available in Supplementary Material 3.

Pre-eruptive Conditions

Mineral compositions in equilibrium with the melt were used to obtain the pressure and temperature before eruption. In the lack of melt inclusions, the average glass composition of each sample together with that of cores and rims was used (Supplementary Material 2). Only for the case of AM030315 was equilibrium reached with the bulk rock composition of McGee et al. (2017). Plagioclase thermometry (Table 2; Putirka 2008, Eq. 24) shows the highest mean temperatures for the mixed avalanche sample (range 1136–1140 °C; from sieved Pl crystals), while the lava fountain lapilli and bomb display lower *T* (from 1105–1114 °C). The December 2015 and February 2017 samples have similar *T* of ca. 1110–1115 °C. This method has a standard error of estimate (SEE) of 36 °C. We identify two dominant pressures using the plagioclase-melt barometer (Eq. 26 of Putirka 2008) (Fig. 6a; Table 2), which has a SEE of 2.8 kbar in our samples. The first extends from 0.2 ± 0.3 to 1.2 ± 0.6 kbar, with a higher *P* for the 2015 lava fountain bomb; all the post-lava fountain samples have *P* below 0.6 ± 0.1 kbar. The second cluster is only constituted by sieve plagioclase from lava fountain mixed avalanche blocks from 3.5 ± 0.7 to 4.0 ± 0.2 kbar. Following the crustal density model for the southern Andes of Tassara et al. (2006) (Fig. 6a), the first range of P values is roughly equivalent to depths of 0 to ~ 5.3 km, and the second from ~ 9.4 to ~ 16.3 km.

Generally, olivine phenocrysts show higher mean *T* for the 3 March 2015 lava fountain event compared to subsequent activity (Table 2; Fig. 6b). Equation 22 of Putirka (2008) returns *T* in the range of ~ 1135 to ~ 1144 °C for the paroxysm, and ~ 1112 to ~ 1117 °C for all other samples. The SEE is 29 °C. Temperatures obtained with the Beattie (1993) and Sisson and Grove (1993) thermometers are slightly higher and lower, respectively, than those of Putirka (2008) (Table 2). Rim and core temperatures usually overlap with or vary within the SEE (Table 2).

We obtained *T* and *P* only for two clinopyroxene compositions following Eq. 33 of Putirka (2008) and Neave and Putirka (2017) barometer; *T* are 1143 and 1150 °C for the paroxysm and the 15th of December 2015 lapilli, respectively (SEE of 42 °C). The *P* values are respectively 2.8 and 3.8 kbar (Fig. 6a), with a SEE of 1.6 kbar.

Water content estimates (Table 2) using the Waters and Lange (2015) hygrometer result in similar average values of c. 1 wt.% for the 2015–2017 samples. Paroxysmal samples show a wider range of H_2O from 0.7 to 1.4 wt.% compared to the post-paroxysm samples (0.9–1.1 wt.% H_2O).

Discussion

Thermodynamic Modelling

We performed thermodynamic modelling using the freeware Rhyolite-MELTS (MELTS version 1.0.2, Ghiorso and Sack 1995; Gualda et al. 2012), to reproduce the compositions of plagioclase phenocryst ($An_{68\text{-}86}$) phases using two different initial compositions (Supplementary Material 2). The first melt composition was obtained by averaging the glass composition from the lapilli erupted on the 9th of December 2015 (54.2 wt.%SiO_2, Mg# 44), which would represent the final stage of evolution of the system and hence the evolved melt from the background activity. The second melt composition is the whole-rock composition of the 2015 lava fountain (sample Vill-15 of McGee et al. 2017; 52.7 wt.%SiO_2, Mg# 53), which would be representative of the system prior to the paroxysm (and likely before phenocryst crystallization).

For our modelling, we used a range of magmatic conditions for *T* (950−1200 °C), *P* (up to 10 kbar), fO_2 (from QFM to ΔQFM + 1 buffer patches) and dissolved H_2O (0−5 wt. %). These ranges are based on analyses obtained of eruptive products of Villarrica by Lohmar et al. (2012), Pioli et al. (2015), Morgado et al. (2015), Pizarro et al. (2019), as well as here. We considered only the modelling results related to ≤ 30 wt.% of solid phases, which would represent crystallisation in equilibrium.

For the December 2015 glass composition, we could only reproduce the $An_{68\text{–}77}$ plagioclase at temperatures of 985–1120 °C and pressures up to 3 kbar (Fig. 7a), and $Fo_{70\text{–}72}$ olivine at temperatures of 1000–1100 °C and pressures up to 2.6 kbar (Fig. 7b). We could not reproduce the $An_{78\text{–}86}$ plagioclase and ~ Fo_{85} olivine as observed in the mixed avalanche sample, by using the glass composition. In contrast, using the more primitive whole-rock composition, we reproduced almost all compositions of plagioclase phenocrysts ($An_{68\text{–}86}$) between 1000–1120 °C and up to 5.3 kbar (Fig. 7a), as well as a large range of olivine compositions ($Fo_{70\text{-}82}$) between 1000–1170 °C and up to 4.2 kbar (Fig. 7b). However, the cores of olivine phenocrysts ($Fo_{\sim 85}$) were not reproduceable, so we interpret them as antecrysts. Thus, we interpret the most evolved plagioclase phenocryst compositions ($An_{68\text{–}77}$) as being crystallised in the upper crust from the carrier melt, while a melt of equivalent composition to that of the whole-rock may have crystallised the primitive plagioclases and/or their core compositions ($An_{78\text{–}86}$). Crystallisation near-equilibrium (with restricted fractional crystallisation) from a melt similar to that of the glass composition may have acted in the upper crust (up to 3 kbar pressure). We note that the presence of olivine antecrysts suggests

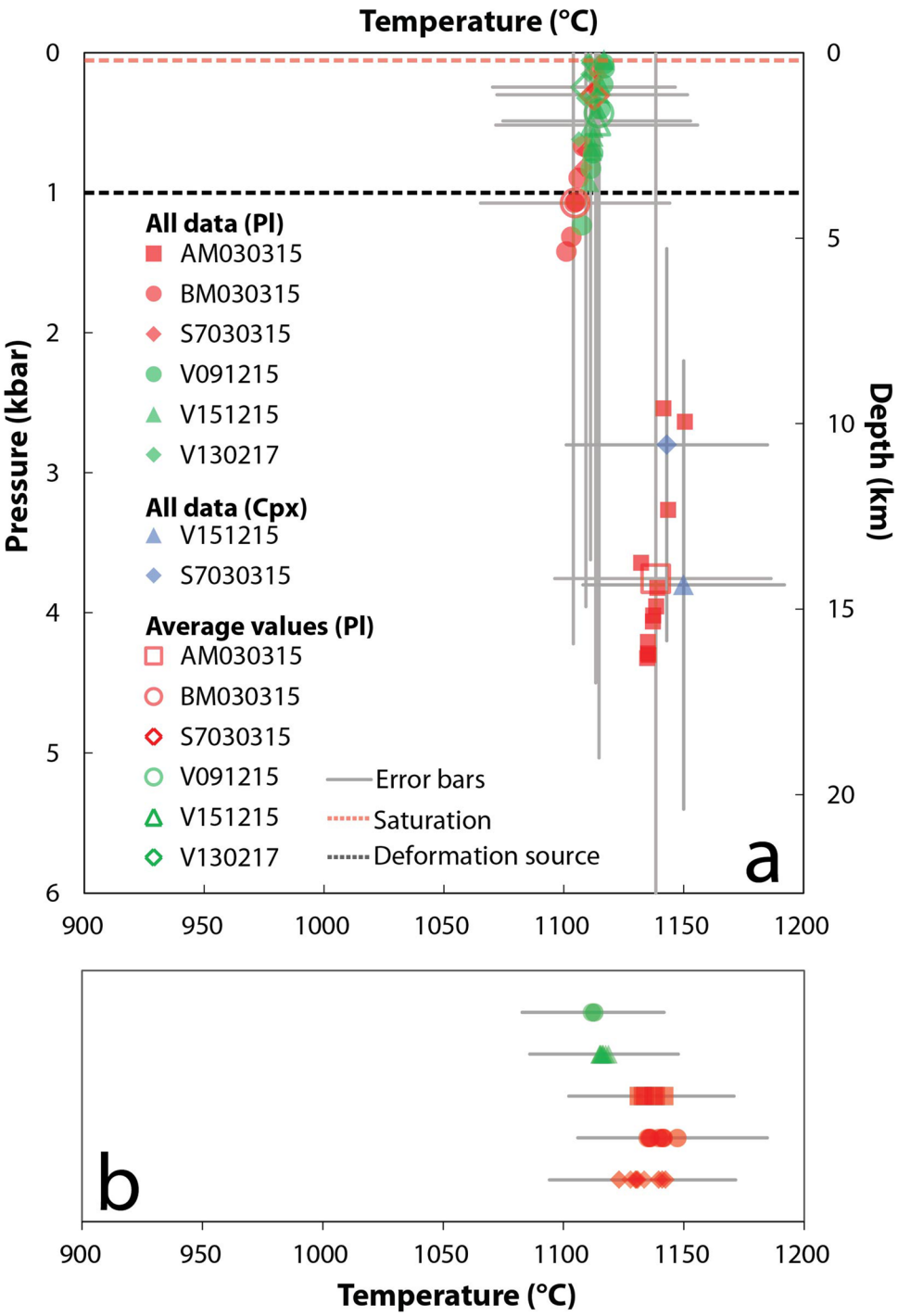

Fig. 6 Pre-eruptive conditions of the 2015–2017 products of Villarrica volcano. **a** Crystallisation temperatures of plagioclase and pyroxene phenocrysts using the plagioclase-liquid and clinopyroxene-liquid geothermobarometers (Putirka 2008; Neave and Putirka 2017). **b** Crystallisation temperatures for olivine by using the olivine-liquid thermometer (Putirka 2008). The dashed line shows the deformation source obtained from Delgado et al. (2017). Core and rim estimates are undifferentiated due to their overlap or small standard deviation (Table 2)

fractional crystallisation in an early stage of magmatic evolution, at pressures exceeding 3 kbar. Morgado et al. (2015) also interpreted $Fo_{\sim 85}$ olivine phenocrysts cores as mid-to-lower crust antecrysts for the 1971 eruption products. This evidence may also indicate deep magma recharge or cryptic mixing. On the other hand, the high variability of the mixed avalanche glasses may indicate either a post-depositional quenching process resulting from the instantaneous interaction of these products with the snow or cryptic magma mixing at depth. Hence, a more detailed assessment of these antecrysts and glass compositions of the samples showing disequilibrium is needed to completely understand the mid-to-lower crust processes before the eruption.

Successful iterations using MELTS yielded the viscosity of the system for glass and melt compositions. In both cases, the probability density functions indicate the most likely range for viscosity is from 10^2 to 10^3 Pa·s (Fig. 8).

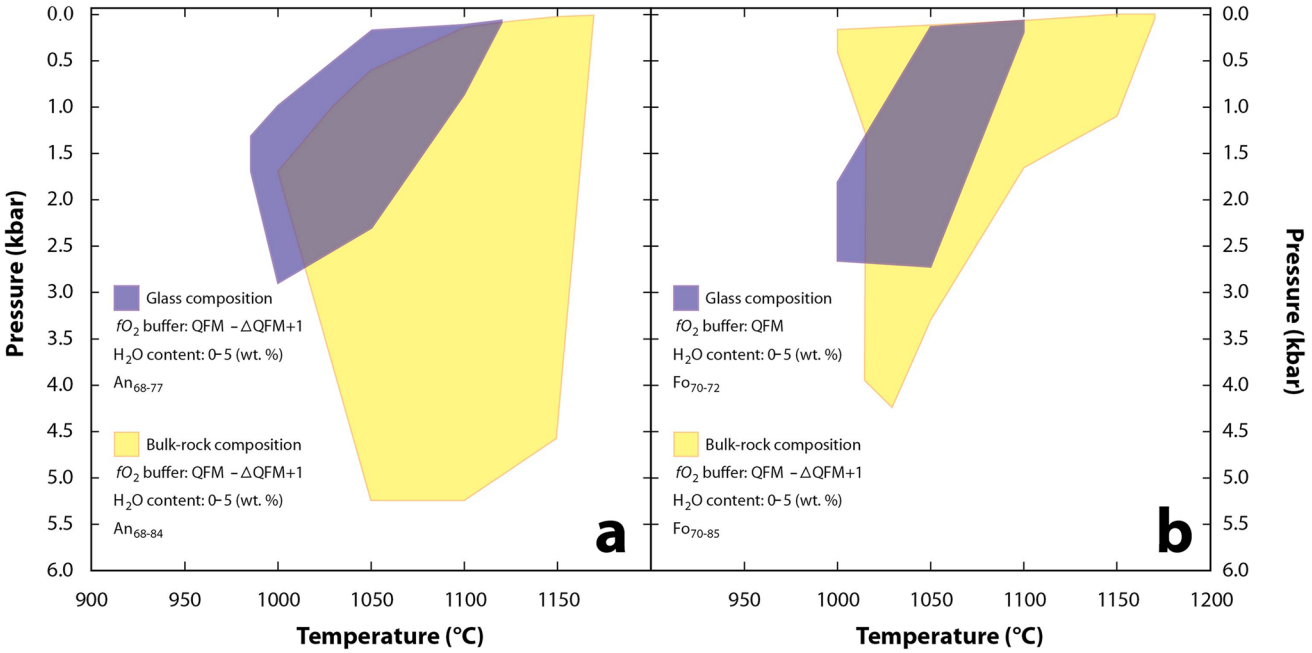

Fig. 7 **a** Calculated stability field of Pl phenocryst compositions obtained via Rhyolite-MELTS considering initial composition melts of glass (An_{68-77}) and whole-rock chemistry (An_{68-84}). Water contents were constrained with the hygrometer-thermometer of Waters and Lange (2015) considering a pressure of 1 kbar (dashed line), based on the deformation observed after the eruption (Delgado et al. 2017). **b** Calculated stability field of olivine phenocrysts using Rhyolite-MELTS (same conditions as for Pl)

This range of likely viscosities is consistent with that obtained by combining the Giordano et al. (2008) model and Roscoe's (1952) equation for a basaltic bomb from the nearby volcanic system of Caburgua, which yielded a viscosity of ~ 400 Pa·s (Morgado et al. 2017).

Comparisons to "Background" and Past Eruptive Products

The bulk rock compositions of historic lava flows (1971, 1984, 1999 and 2004) have similar SiO_2 contents between 52 and 54 wt.% (Fig. 3a–c). These show lower SiO_2 and higher MgO contents than the majority of 2015–2017 products (52–56 wt.% SiO_2; Fig. 3d–h). This suggests that the 2015–2017 products represent slightly more differentiated liquids.

Our plagioclase compositions are normally distributed around $An_{\sim 75}$, which is the dominant composition of plagioclase in historic Villarrica products (i.e., 1921, 1948 and 1971; Pizarro et al. 2019; Boschetty et al. 2022). However, plagioclase compositions show a larger range in An contents for the lava fountain samples (An_{66-86}), compared to the post-lava fountain products (An_{70-82}; Fig. 4a). In addition, the products of the 2015 fountain contain olivine with a large range of Fo contents (Fo_{75-78}) than the post eruptions (Fo_{74-75}; Fig. 4b). Compared to the products of historic eruptions, Pizarro et al. (2019) report overlapping but slightly higher Fo-contents (Fo_{71-83}). Both the lava fountain and the subsequent volcanic products contain scarce clinopyroxene, which is a characteristic shared with other twenty-first century eruptions of Villarrica (Witter et al. 2004). The composition of the few measured clinopyroxenes is similar to that of historic eruptions (En_{47-52}, Wo_{48-43} and Fs_{10-15}; Pizarro et al. 2019). All these comparisons agree with compositional trends identified by Boschetty et al. (2022) based on products erupted throughout Villarrica's entire post-glacial history.

The work of Morgado et al. (2015) determined two storage regions for the 1971 eruption using olivine-augite pairs: a deep-seated reservoir at 6.3–8.1 kbar (equivalent to depths from 35 to 19 km) and at ca. 1200 °C, and a second shallower region to ≤ 1.4 kbar (equivalent to depths ≤ 5.3 km) and at ca. 1170 °C. Pizarro et al. (2019) used olivine-clinopyroxene clots to obtain P–T conditions for several twentieth century eruptions, resulting in two clusters centred ~ 0.6 kbar and ~ 1170 °C, and ~3.4 and 1190 °C. Despite the large uncertainty of Pl-liq barometry (Putirka 2008), our pressures and minimum olivine temperatures fit well with both the shallower and deeper storage zones of Pizarro et al. (2019). In addition, their equilibrium temperatures of Pl-Ol-Cpx at

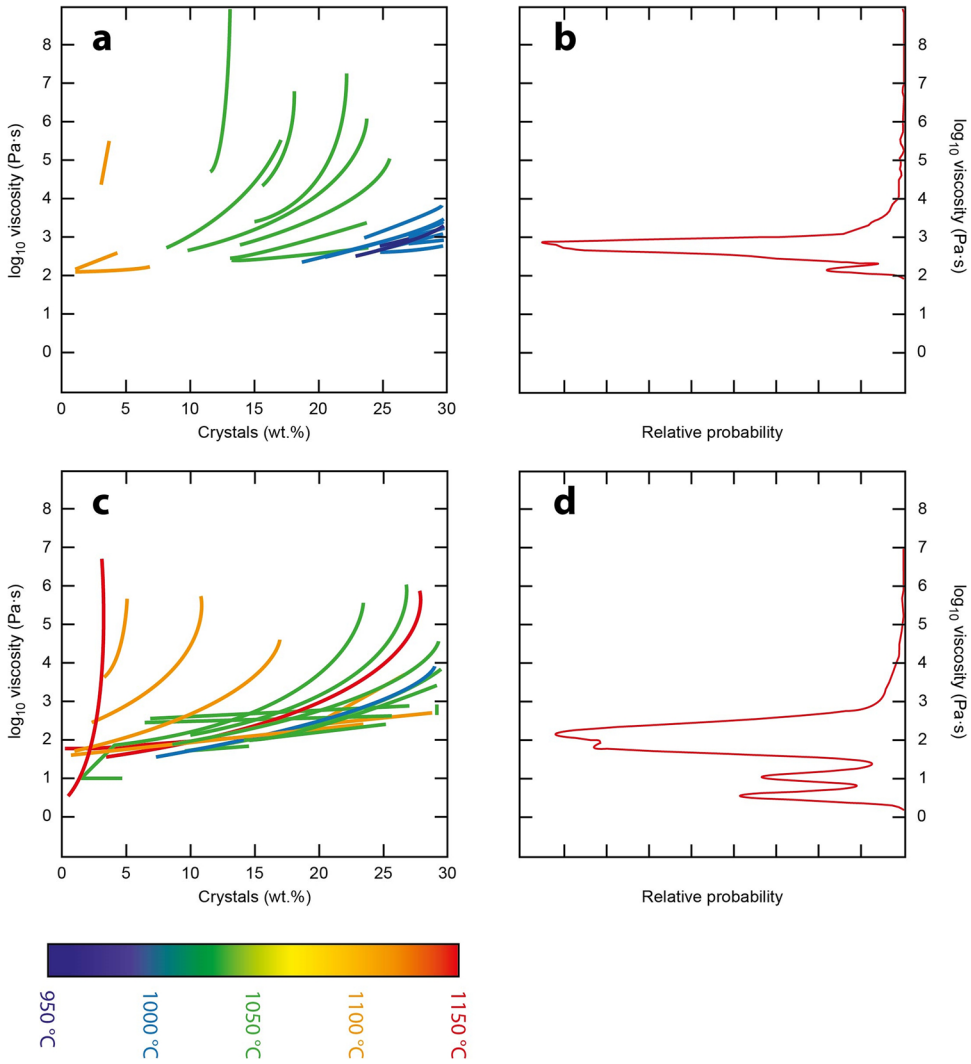

Fig. 8 Viscosity vs crystals (wt. %) plots according to MELTS modelling for glass composition (**a**) and whole-rock composition (**c**) considering different magmatic temperatures (from 950 to 1150 °C) and initial water contents (from 1 to 5 wt. %). The kernel density estimation of probability distributions of all modelled viscosities suggests a maximum probability from 10^2 to 10^3 Pa·s for glass (**b**) and from $10^{1.5}$ to 10^2 Pa·s for whole rock

about 1090 °C, largely fit with our Pl-liq constraints. Moreover, the post-2015 Villarrica edifice uplift was sourced at 4.2 ± 0.1 km deep (Delgado et al. 2017), consistent with the refilling of a shallower storage zone. Our estimates suggest that magmas are stored and crystallise throughout the mid-upper crust, again in agreement with the results of the thermodynamic modelling of Boschetty et al. (2022). In addition, long-term fractional crystallisation may have occurred in the mid-to-lower crust, and near-equilibrium crystallisation dominated the late stage of magmatic evolution at $P < 3$ kbar.

Our estimates of melt H_2O-contents (ca. 1 wt.%) are higher than those obtained for the scoria erupted at Villarrica between 1984 and 2004 (0.1 ± 0.6 wt%; Witter et al. 2004; Gurioli et al. 2008). Higher water contents have been reported in melt inclusions from the Chaimilla fallout deposit (1.7–3.1 wt.%; Pioli et al. 2015) and the Los Nevados parasitic cones (0.3–3.0 wt.%; Robidoux et al. 2021), and from modelling of the Licán ignimbrite (0.5–3.2 wt.%; Lohmar et al. 2012). Plagioclase may record the entire crystallization and ascent history of the magma (Blundy and Cashman 2008), thus providing variable values for *P*, *T* and H_2O as shown in Fig. 6a. In contrast, glass compositions likely represent degassed erupted carrier liquids; thus, their H_2O contents can be considered as a minimum. As Villarrica is characterised by open conduit degassing (Palma et al. 2008; Aiuppa et al. 2017) the H_2O reported by Witter et al. (2004) and Gurioli et al. (2008) likely represents the degassed magma near the top of the conduit, which is common at such systems, for example, Stromboli (Gurioli et al. 2014).

Triggering Mechanism

We observe normal zoning in crystal phases (i.e., plagioclase and olivine phenocrysts), equilibrium between most of crystal rims and the residual melt, as well as very slight variations in the chemical trends between bulk rock compositions

and the residual melt. Slight incompatible trace element depletion is observed in bulk rock compositions, with respect to glass. On the other hand, thermodynamic modelling (MELTS) indicates mostly equilibrium conditions for plagioclase and olivine at $P < 3$ kbar. Hence, fractional crystallisation, if present, should have occurred at greater depths (ca. ≤ 11 km).

There is no amphibole in the 2015–2017 mineral assemblages. This can be indicative of slow decompression, as amphibole is unstable under these conditions (Rutherford and Hill 1993; Shea and Hammer 2013). A slow buoyant ascent of the magma from the shallow crust via the open conduit system of Villarrica would also explain LP seismicity and magmatic degassing 1 month before the eruption, as well as the lack of deformation (e.g., Delgado et al. 2017; Delgado et al. 2022). This is also consistent with the lack of volcano-tectonic seismicity, usually interpreted to be due to overpressure and rock fracturing along magmatic pathways associated with a magma ascent intrusion in a closed system.

Buoyant magma ascent could occur coupled with overpressure of a deeper storage region (i.e., 4–6 km depth). Then, volatile exsolution may have triggered accelerated magma ascent, overpressure and fragmentation at shallower levels (< 0.8 km depth) following a "first boiling"-like behaviour. Also, according to our MELTS modelling, the density of the magma (considering melt and phenocrysts) is lower than the value of 2700 kg/m^3 reported for the upper crust by Tassara et al. (2006) (Fig. 9). Therefore, we favour the buoyant ascent as the main process controlling magma ascent. Aiuppa et al. (2017) observed anomalously high CO_2/SO_2 starting 1 month before the eruption. They propose that separate ascent of over-pressured gas bubbles, originating from at least 20–35 MPa, was the driver for activity escalation toward the 3 March 2015 climax. These pressures are consistent with depths of 0.9 to 1.3 km, which represent the H_2O-saturation depth for the 2015 magma (considering 1 wt.% H_2O). To confirm this, we used the glass chemistry of the 2015 lava fountain lapilli and bomb, their

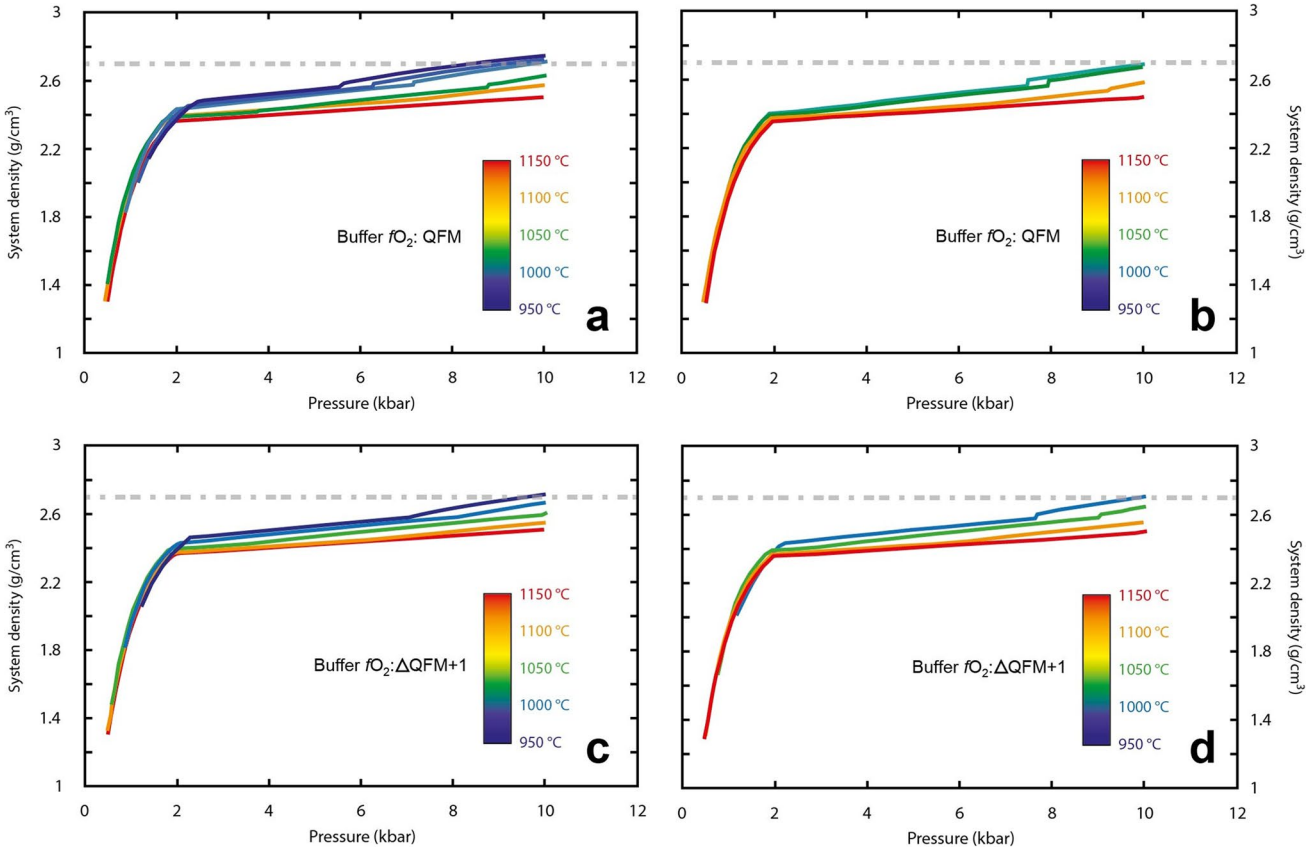

Fig. 9 System density (g·cm^{-3}) vs pressure (kbar) plot according to MELTS modelling considering glass and whole-rock compositions and assuming a water-saturated magma for temperatures from 950 to 1150 °C. The solid lines represent the modellings at different magmatic temperatures and the dashed lines represent the density of the upper crust (2.7 g·cm^{-3}; Tassara et al. 2006). **a** shows glass composition modelling considering QFM oxygen fugacity buffer, **b** shows whole-rock composition modelling considering QFM oxygen fugacity buffer, **c** shows glass modellings considering ΔQFM + 1 oxygen fugacity buffer, and **d** shows glass modelling considering ΔQFM + 1 oxygen fugacity buffer

respective temperatures and H_2O contents (Table 2) to run MagmaSat (Ghiorso and Gualda 2015), as implemented in VESIcal (v.1.2.0; Iacovino et al. 2021). Using this model, we obtained saturation pressures of ca. 0.21 and 0.06 kbar (i.e., depths of 0.8 and 0.2 km), respectively. Witter et al. (2004) also calculated saturation at < 0.3 kbar from samples of the 1999–2004 eruptions, while Pioli et al. (2015) obtained higher depths (0.7–0.3 kbar) for the Chaimilla eruption, where both studies used melt inclusions. As previously observed by Witter et al. (2004) using MELTS, Rhyolite-MELTS modelling yields < 2% olivine crystallization at lower depths, as well as stable crystallisation of $An_{<75}$ Pl rims with degassed magma conditions, as in our samples (Table 1). Evidence supporting rapid pressurization of the upper part of the conduit (< 1 km depth) is also given by trace elements in olivine crystals. As Ni and Cr are compatible elements, they are preferentially incorporated into early-forming minerals, in contrast to Li which is moderately incompatible in olivine (Grant and Wood 2010). We observed increasing Li but decreasing Ni and Cr in the rims of olivine. Parkinson et al. (2007) interpreted increased Li in olivine and pyroxene rims, 4–8 times higher than in the core, to result from fractionation. We measured five-times higher Li concentrations in low Fo olivine rims, with respect to the cores. As Villarrica's magma contains primitive melt inclusions in plagioclase with high levels of chlorine (up to 2090 ppm; Zajacz and Halter 2009), its rapid extraction into vapour phase may affect Li diffusion as Li forms hydroxides in the absence of chlorine (Yamaguchi et al. 2010). Hence, a fast migration of Li between melt, crystals and vapour phases may explain these trends. These phenomena have been previously observed at Stromboli volcano (Italy) by Viccaro et al. (2021). The phenomenon suggests gas accumulation and re-incorporation of Li at very low pressure just prior the onset of a paroxysm Viccaro et al. (2021).

Together, all these lines of evidence suggest that the source magma for the 2015 lava fountain mostly evolved in equilibrium during buoyant ascent, before saturation and acceleration near the surface through a "first boiling"-like event. At analogous open conduit systems, such as Stromboli, paroxysms have been also explained by the ascent of a CO_2/H_2O–rich slug enveloped by melt from depth (6–9 km), in a quasi–closed system, triggering magma fragmentation (Métrich et al. 2021). These deep, bubbly magmas are able to ascend at fast rates (1–2 m/s) to interact with more crystalised shallow magma, producing mixing and eruption (Pichavant et al. 2022). Recent research shows that magma fragmentation within lava fountains may occur once the magma is ejected from the vent, as triggered by further volatile expansion to generate fine ash. This is mostly the case of "higher" viscosity basaltic magmas such as those of arc settings (La Spina et al. 2021). A similar trigger has been suggested for Etna (Italy; Zuccarello et al. 2021). Most of the twentieth century eruptions of Villarrica have been interpreted as being produced by cryptic mixing between compositionally similar mafic magmas (Pizarro et al. 2019). These historic eruptions have ranged from effusive to moderately explosive (VEI 0 to 3), producing small pyroclastic flows, extensive lava flows (extending up to 20 km downslope) and tephra fallout (Moreno and Clavero 2006). Conversely, the March 2015 lava fountain was dominantly explosive and short-lasting. Given the high compositional variability of the AM030315 glasses, in addition to the disequilibrium textures observed in the same sample, we should not discard these kinds of processes also occurring at depth to trigger rarer, but more highly explosive, activity. This, like at Stromboli (Pichavant et al. 2022), Yasur (Kremers et al. 2012), Pacaya (Mari 2015), for example, punctuates the "normal" activity. For example, Pacaya went through cycles of building Strombolian activity to culminate in a short but highly explosive, paroxysmal event in 2010 (Wardman et al 2012).

Volcanic Hazard Considerations

Villarrica is not only the most active volcano in Chile (Petit-Breuilh and Lobato 1994; Moreno and Clavero 2006) but is also the highest-risk volcano in the country (SERNAGEOMIN 2020) due to the exposure of a large population and critical infrastructure (e.g., the cities of Villarrica, Pucón, Licán Ray and Coñaripe). The 3 of March lava fountaining event was characterised by a rapid evolution from Strombolian activity to intense lava fountaining. Despite the pre-eruptive unrest signals, these rapid eruptive style transitions may pose a challenge for eruption forecasting. Moreover, similar open conduit volcanoes with tholeiitic mafic compositions and low H_2O contents at pre-eruptive conditions, such as Masaya in Nicaragua, have demonstrated to produce Plinian eruptions as magma crystallises and saturates near the surface (Bamber et al. 2020).

Our study provides critical insight to enable improved understanding of this type of activity, previously unstudied at Villarrica volcano. This is especially valuable considering the increasing unrest of Villarrica in late 2022. More studies are required to better understand the timings, depth scales and specific processes related to magma crystallisation, volatile exsolution and overpressure in this open conduit system before, during and after such explosive events. In this respect, experimental petrology may provide further clues as to the drivers of such paroxysmal events, as well as textural studies focused on ascent rates and diffusion chronometry. Moreover, monitoring of gas emissions might provide key precursory signals for future paroxysmal events (Aiuppa et al. 2007; Burton et al. 2007; Allard 2010; Aiuppa et al. 2017; Edmonds et al. 2022).

Conclusions

Our study highlights the importance of studying pyroclastic rocks produced by paroxysmal events at open conduit systems to further the understanding of pre-eruptive conditions and magma evolution processes. The 2015 Villarrica lava fountain was fed from a deeper and hotter basaltic andesite magma (~ 9.4–16.3 km, ca. 1140 °C), which experienced long-term magmatic evolution in near-equilibrium conditions and buoyant ascent in the upper crust (< 3 kbar). Ultimately, the main drivers of the 2015 lava fountain were H_2O saturation and over-pressure at shallow depths (< 0.8 km), triggering magma acceleration and fragmentation. Magma erupted during subsequent small Strombolian explosions following the lava fountain (later in 2015 and early in 2017) was likely sourced from a shallower and colder storage region (≤ 5.3 km; ca. 1110 °C). This contrasts with most of the previously studied twentieth-century eruptions of Villarrica which were likely fed by magma mixing to produce longer-lived eruptions with effusive and milder explosive activity. On the other hand, the triggering mechanisms observed for the 2015 Villarrica lava fountain are like those reported in other open conduit systems, suggesting deeper controls and shallow volatile overpressure during paroxysmal events. Given the rapid escalation from Strombolian explosions to lava fountaining activity, the 2015 Villarrica lava fountain represents challenging conditions for volcano monitoring and eruption forecasting in the future, requiring further research useful for risk assessment and contingency planning.

Supplementary Information The online version contains supplementary material available at https://doi.org/10.1007/s00445-022-01621-0.

Acknowledgements Jorge Romero is financed through NSF-GEONERC-funded project DisEqm (NE/N018575/1), V-PLUS and the Dean's Award of the University of Manchester. This study is part of the '4DVOLC: Magma storage and ascent in volcanic systems via time-resolved HPHT X-ray tomographic experiments and numerical modelling of eruption dynamics' financed by the UK Research and Innovation within the Future Leaders Fellowships scheme (Margherita Polacci). Alessandro Pisello is supported by DAAD-MIUR JMP N. 14103. Felix Boschetty is funded by the National Environmental Research Council (NERC) Panorama Doctoral Training Partnership (DTP) NE/S007458/1. We thank the constructive reviews of Claudia D'Oriano, Guido Giordano, and Editor Ulrich Kueppers, which significantly improved this manuscript. We are grateful to Daniel Basualto and Geo-Araucanía team for providing aerial photos and fruitful discussion. All the Rhyolite-MELTS simulations are available upon request.

References

Aiuppa A, Bitetto M, Francofonte V et al (2017) A CO_2-gas precursor to the March 2015 Villarrica volcano eruption. Geochem Geophys Geosys 18(6):2120–2132. https://doi.org/10.1002/2017GC006892

Aiuppa A, Moretti R, Federico C et al (2007) Forecasting Etna eruptions by real-time observation of volcanic gas composition. Geology 35:1115–1118

Allard P (2010) A CO_2-rich gas trigger of explosive paroxysms at Stromboli basaltic volcano, Italy. J Volcanol Geotherm Res 189:363–374

Andronico D, Del Bello E, D'Oriano C et al (2021) Uncovering the eruptive patterns of the 2019 double paroxysm eruption crisis of Stromboli volcano. Nat Comm 12(1):1–14

Bamber EC, Arzilli F, Polacci M et al (2020) Pre-and syn-eruptive conditions of a basaltic Plinian eruption at Masaya Volcano, Nicaragua: the Masaya Triple Layer (2.1 ka). J Volcanol Geotherm Res 392:106761

Beattie P (1993) Olivine-melt and orthopyroxene-melt equilibria. Contrib to Mineral Petrol 115(1):103–111. https://doi.org/10.1007/BF00712982

Beckett FM, Burton M, Mader H et al (2014) Conduit convection driving persistent degassing at basaltic volcanoes. J Volcanol Geotherm Res 283:19–35

Bertagnini A, Di Roberto A, Pompilio M (2011) Paroxysmal activity at Stromboli: lessons from the past. Bull Volcanol 73:1229–1243. https://doi.org/10.1007/s00445-011-0470-3

Blundy J, Cashman K (2008) Petrologic reconstruction of magmatic system variables and processes. Rev Mineral Geochem 69(1):179–239

Boschetty FO, Ferguson DJ, Cortés JA et al (2022) Insights into magma storage beneath a frequently erupting arc volcano (Villarrica, Chile) from unsupervised machine learning analysis of mineral compositions. Geochem Geophys Geosys e2022GC010333

Breard ECP, Calder ES, Ruth D (2020) The interaction between concentrated pyroclastic density currents and snow: a case study from the 2008 mixed avalanche from Volcán Llaima (Chile). Bull Volcanol 82:75. https://doi.org/10.1007/s00445-020-01413-4

Burton M, Allard P, Muré F, La Spina A (2007) Magmatic gas composition reveals the source depth of slug-driven Strombolian explosive activity. Sci 317:227–230

Coppola D, Laiolo M, Cigolini C et al (2020) Thermal remote sensing for global volcano monitoring: experiences from the MIROVA system. Front Earth Sci 7:362. https://doi.org/10.3389/feart.2019.00362

Cashman KV, Edmonds M (2019) Mafic glass compositions: a record of magma storage conditions, mixing and ascent. Philos Trans R Soc A 377:2139. https://doi.org/10.1098/rsta.2018.0004

Castruccio A, Contreras MA (2016) The influence of effusion rate and rheology on lava flow dynamics and morphology: a case study from the 1971 and 1988–1990 eruptions at Villarrica and Lonquimay volcanoes, Southern Andes of Chile. J Volcanol Geotherm Res 327:469–483

Cioni R, D'Oriano C, Bertagnini A (2008) Fingerprinting ash deposits of small-scale eruptions by their physical and textural features. J Volcanol Geotherm Res 177(1):277–287

Corsaro RA, Miraglia L (2005) Dynamics of 2004–2005 Mt. Etna effusive eruption as inferred from petrologic monitoring. Geophys Res Lett 32(13):L13302

Costantini L, Pioli L, Bonadonna C et al (2011) A late Holocene explosive mafic eruption of Villarrica volcano, Southern Andes: the Chaimilla deposit. J Volcanol Geotherm Res 200(3–4):143–158

Delgado F, Pritchard ME, Ebmeier S et al (2017) Recent unrest (2002–2015) imaged by space geodesy at the highest risk Chilean volcanoes: villarrica, Llaima, and Calbuco (Southern Andes). J Volcanol Geotherm Res 344:270–288. https://doi.org/10.1016/j.jvolgeores.2017.05.020

Delgado F, Contreras-Arratia R, Samsonov S (2022) Magma buoyancy drives rhyolitic eruptions: a tale from the VEI 5 2008–2009 Chaitén eruption (Chile) from seismological and geodetic data. Earth Planet Sci Lett 590:117564

Dellino P, Gudmundsson MT, Larsen G et al (2012) Ash from the Eyjafjallajokull eruption (Iceland): fragmentation processes and aerodynamic behavior. J Geophys Res-Sol Ea 117:B00C04. https://doi.org/10.1029/2011JB008726

Droop GTR (1987) A general equation for estimating Fe3+ concentrations in ferromagnesian silicates and oxides from microprobe analyses, using stoichiometric criteria. Mineral Mag 51(361):431–435. https://doi.org/10.1180/minmag.1987.051.361.10

Edmonds M, Liu E, Cashman K (2022) Open-vent volcanoes fuelled by depth-integrated magma degassing. Bull Volcanol 84:28. https://doi.org/10.1007/s00445-021-01522-8

Edwards B, Palma J, Vera F et al (2018) Origins and implications of mixed avalanche deposits from the 3 March 2015 eruption of Villarrica volcano, Chile. Proceedings from the 20th EGU General Assembly, 4-13 April, Vienna, Austria, p 11090

Gavrilenko M, Herzberg C, Vidito C et al (2016) A calcium-in-olivine geohygrometer and its application to subduction zone magmatism. J Petrol 57(9):1811–1832

Giordano G, De Astis G (2021) The summer 2019 basaltic Vulcanian eruptions (paroxysms) of Stromboli. Bull Volcanol 83(1):1–27

Giordano D, Russell JK, Dingwell DB (2008) Viscosity of magmatic liquids: a model. Earth Planet Sc Lett 271(1–4):123–134

Ghiorso MS, Gualda GA (2015) An H_2O–CO_2 mixed fluid saturation model compatible with rhyolite-MELTS. Contrib Mineral Petrol 169:53

Ghiorso MS, Sack RO (1995) Chemical mass transfer in magmatic processes IV. A revised and internally consistent thermodynamic model for the interpolation and extrapolation of liquid-solid equilibria in magmatic systems at elevated temperatures and pressures. Contrib Mineral Petrol 119(2):197–212

Grant KJ, Wood BJ (2010) Experimental study of the incorporation of Li, Sc, Al and other trace elements into olivine. Geochim Cosmochim Acta 74(8):2412–2428

Gurioli L, Harris AJL, Houghton BF et al (2008) Textural and geophysical characterization of explosive basaltic activity at Villarrica volcano. J Geophys Res: Solid Earth 113:B8206

Gurioli L, Coló L, Bollasina AJ et al (2014) Dynamics of Strombolian explosions: inferences from field and laboratory studies of erupted bombs from Stromboli volcano. J Geophys Res: Solid Earth 119:319–345

Gualda GA, Ghiorso MS, Lemons RV, Carley TL (2012) Rhyolite-MELTS: a modified calibration of MELTS optimized for silica-rich, fluid-bearing magmatic systems. J Petrol 53(5):875–890

Heiken G (1972) Morphology and petrography of volcanic ashes. Geol Soc Am Bull 83(7):1961–1988

Hickey-Vargas R, Moreno H, López-Escobar L, Frey FA (1989) Geochemical variations in Andean basaltic and silicic lavas from the Villarrica-Lanin volcanic chain (39.5 S): an evaluation of source heterogeneity, fractional crystallization and crustal assimilation. Contrib Mineral Petrol 103(3):361–386

Iacovino K, Matthews S, Wieser PE et al (2021) VESIcal Part I: an open-source thermodynamic model engine for mixed volatile (H2O-CO2) solubility in silicate melts. Earth Space Sci 8(11):e2020EA001584

Jenner FE (2017) Cumulate causes for the low contents of sulfide-loving elements in the continental crust. Nat Geosci 10(7):524–529

Johnson J, Palma JL (2015) Lahar infrasound associated with Volcán Villarrica's 3 March 2015 eruption. Geophys Res Lett 42:6324–6331. https://doi.org/10.1002/2015GL065024

Johnson JB, Watson LM, Palma JL et al (2018) Forecasting the eruption of an open-vent volcano using resonant infrasound tones. Geophys Res Lett 45:2213–2220. https://doi.org/10.1002/2017GL076506

Kremers S, Lavallée Y, Hanson J et al (2012) Shallow magma-mingling-driven Strombolian eruptions at Mt. Yasur volcano, Vanuatu. Geophys Res Lett 39(21):L21304 https://doi.org/10.1029/2012GL053312

Kress VC, Carmichael ISE (1991) The compressibility of silicate liquids containing Fe2O3 and the effect of composition, temperature, oxygen fugacity and pressure on their redox states. Contrib to Mineral and Petrol 108(1–2):82–92. https://doi.org/10.1007/BF00307328

La Spina G, Arzilli F, Llewellin EW et al (2021) Explosivity of basaltic lava fountains is controlled by magma rheology, ascent rate and outgassing. Earth Planet Sci Lett 553:116658

Lerner AH, Wallace PJ, Shea T et al (2021) The petrologic and degassing behavior of sulfur and other magmatic volatiles from the 2018 eruption of Kīlauea, Hawai'i: melt concentrations, magma storage depths, and magma recycling. Bull Volcanol 83:43

Lohmar S, Parada M, Gutiérrez F (2012) Mineralogical and numerical approaches to establish the pre-eruptive conditions of the mafic Lican Ignimbrite, Villarrica Volcano (Chilean Southern Andes). J Volcanol Geotherm Res 235:55–69

Luhr JF, Carmichael IS (1990) Petrological monitoring of cyclical eruptive activity at Volcán Colima, México. J Volcanol Geotherm Res 42(3):235–260

Lyons JJ, Waite GP, Rose WI, Chigna G (2010) Patterns in open vent, strombolian behavior at Fuego volcano, Guatemala, 2005–2007. Bull Volcanol 72(1):1–15

Mari N (2015) Insights into the relationship between mixing duration and Volcanic Explosivity Index (VEI): Pacaya and Fuego volcanoes, Guatemala (Open Access Master's Thesis, Michigan Technological University, 2015)

McDonough WF, Sun SS, Ringwood AE, Jagoutz E, Hofmann AW (1992) Potassium, rubidium, and cesium in the Earth and Moon and the evolution of the mantle of the Earth. Geochimica et Cosmochimica Acta 56(3):1001–1012

McGee LE, Brahm R, Rowe MC et al (2017) A geochemical approach to distinguishing competing tectono-magmatic processes preserved in small eruptive centres. Contrib to Mineral Petrol 172(6):44. https://doi.org/10.1007/s00410-017-1360-2

Métrich N, Bertagnini A, Pistolesi M (2021) Paroxysms at Stromboli volcano (Italy): source, genesis and dynamics. Front Earth Sci 9:593339. https://doi.org/10.3389/feart.2021.593339

Moreno H, Clavero J (2006) Geología del área del volcán Villarrica, Regiones de la Araucanía y de los Lagos. Servicio Nacional de Geología y Minería, Carta Geológica de Chile, Serie Geología Básica 98:21

Moreno H, Toloza V (2015) The large tephra fall deposits related to the ca. 3.500 BP Pucón eruption: an unexpected revelation, Villarrica volcano, Southern Andes 39.4 S, Chile. In Proceedings of the XIV Congreso Geológico Chileno 1:570–573

Morgado E, Parada MA, Contreras C et al (2015) Contrasting records from mantle to surface of Holocene lavas of two nearby arc volcanic complexes: Caburgua-Huelemolle Small Eruptive Centers and Villarrica Volcano, Southern Chile. J Volcanol Geotherm Res 306:1–16

Morgado E, Parada MA, Morgan DJ et al (2017) Transient shallow reservoirs beneath small eruptive centres: constraints from Mg-Fe interdiffusion in olivine. J Volcanol Geotherm Res 347:327–336

Morgavi D, Arienzo I, Montagna C, Perugini D, Dingwell DB (2017) Magma mixing: history and dynamics of an eruption trigger. In Volcanic Unrest: from science to society, eds Gottsmann J, Neuberg J, Scheu B (eds) Springer, Switzerland, pp 123–137

Moussallam Y, Edmonds M, Scaillet B et al (2016) The impact of degassing on the oxidation state of basaltic magmas: a case study of Kīlauea volcano. Earth Planet Sci Lett 450:317–325

Naranjo JA, Moreno H (2004) Laharic debris-flows from Villarrica Volcano. In: Lara LE, Clavero J (eds) Villarrica Volcano (39.5°S), Southern Andes, Chile. Servicio Nacional de Geología y Minería. Boletín 61:28–38

Neave DA, Putirka KD (2017) A new clinopyroxene-liquid barometer, and implications for magma storage pressures under Icelandic rift zones. Am Mineral 102(4):777–794. https://doi.org/10.2138/am-2017-5968

Palma JL, Calder ES, Basualto D et al (2008) Correlations between SO2 flux, seismicity, and outgassing activity at the open vent of Villarrica volcano. Chile J Geophys Res Solid Earth 113:B10201. https://doi.org/10.1029/2008JB005577

Parkinson IJ, Hammond SJ, James RH, Rogers NW (2007) High-temperature lithium isotope fractionation: Insights from lithium isotope diffusion in magmatic systems. Earth Planet Sci Lett 257(3–4):609–621

Patrick M, Swanson D, Orr T (2019) A review of controls on lava lake level: insights from Halema ʻuma ʻu Crater, Kīlauea Volcano. Bull Volcanol 81(3):13

Petit-Breuihl M, Lobato J (1994) Análisis comparativo de la cronología eruptiva histórica de los volcanes Llaima y Villarrica. In: Proceedings of the Congreso Geológico Chileno No. 7, Concepción, Chile, pp 366–370

Pichavant M, Di Carlo I, Pompilio M et al (2022) Timescales and mechanisms of paroxysm initiation at Stromboli volcano, Aeolian Islands, Italy. Bull Volcanol 84:36

Pioli L, Pistolesi M, Rosi M (2014) Transient explosions at open-vent volcanoes: the case of Stromboli (Italy). Geol 42(10):863–866

Pioli L, Scalisi L, Costantini L et al (2015) Explosive style, magma degassing and evolution in the Chaimilla eruption, Villarrica volcano, Southern Andes. Bull Volcanol 77(11):1–14

Pizarro C, Parada MA, Contreras C, Morgado E (2019) Cryptic magma recharge associated with the most voluminous 20th century eruptions (1921, 1948 and 1971) at Villarrica Volcano. J Volcanol Geotherm Res 384:48–63

Putirka KD (2005) Igneous thermometers and barometers based on plagioclase + liquid equilibria: tests of some existing models and new calibrations. Am Miner 90(2–3):336–346. https://doi.org/10.2138/am.2005.1449

Putirka KD (2008) Thermometers and barometers for volcanic systems. Rev Mineral Geochem 69(1):61–120. https://doi.org/10.2138/rmg.2008.69.3

Re G, Corsaro RA, D'Orianoa C, Pompilio M (2021) Petrological monitoring of active volcanoes: a review of existing procedures to achieve best practices and operative protocols during eruptions. J Volcanol Geotherm Res 419:107365

Rhodes JM, Dungan MA, Blanchard DP, Long PE (1979) Magma mixing at mid-ocean ridges: evidence from basalts drilled near 22° N on the Mid-Atlantic Ridge. Tectonophysics 55(1):35–61. https://doi.org/10.1016/0040-1951(79)90334-2

Robidoux P, Pastén D, Levresse G et al (2021) Volatile content implications of increasing explosivity of the Strombolian eruptive style along the fracture opening on the NE Villarrica Flank: minor eruptive centers in the Los Nevados group 2. Geosciences 11(8):309. https://doi.org/10.3390/geosciences11080309

Roduit N (2008) JMicroVision: Image analysis toolbox for measuring and quantifying components of high-definition images. Ver 1(7):2002–2007

Roeder PL, Emslie RF (1970) Olivine-liquid equilibrium. Contrib Miner Petrol 29(4):275–289. https://doi.org/10.1007/BF00371276

Romero JE, Vera F, Polacci M et al (2018) Tephra from the 3 March 2015 sustained column related to explosive lava fountain activity at Volcán Villarrica (Chile). Front Earth Sci 6:98

Romero JE, Burton M, Cáceres F et al (2022) The initial phase of the 2021 Cumbre Vieja ridge eruption (Canary Islands): products and dynamics controlling edifice growth and collapse. J Volcanol Geotherm Res 431:107642

Roscoe R (1952) The viscosity of suspensions of rigid spheres. Br J Appl Phys 3(8):267–269

Rose WI, Palma JL, Delgado Granados H, Varley N (2013) Open-vent volcanisms and related hazards: Overview. Amer Geol Soc Spec Paper 498:vi–xiii. https://doi.org/10.1130/2013.2498(00)

Ross PS, Dürig T, Comida PP et al (2022) Standardized analysis of juvenile pyroclasts in comparative studies of primary magma fragmentation; 1. Overview and workflow. Bull Volcanol 84:13. https://doi.org/10.1007/s00445-021-01516-6

Rutherford MJ, Hill PM (1993) Magma ascent rates from amphibole breakdown: an experimental study applied to the 1980–1986 Mount St. Helens eruptions. J Geophys Res: Solid Earth 98(B11):19667–19685

Schmith J, Höskuldsson Á, Holm PM (2017) Grain shape of basaltic ash populations: implications for fragmentation. Bull Volcanol 79(2):14

SERNAGEOMIN (2015) Reporte de Actividad Volcánica (RAV), Región de la Araucanía, Año 2015 Diciembre – Volumen 110. Red Nacional de Vigilancia Volcánica, Observatorio Volcanológico de los Andes del Sur, 6 p. Available at: http://sitiohistorico.sernageomin.cl/reportesVolcanes/201601031141479RAV_Araucania_2015_diciembre_vol_110.pdf. Accessed 28 Jan 2022

SERNAGEOMIN (2017) Reporte de Actividad Volcánica (RAV) N°2, Febrero 2017, Región de la Araucanía. Red Nacional de Vigilancia Volcánica, Observatorio Volcanológico de los Andes del Sur, 9 p. Available at: http://sitiohistorico.sernageomin.cl/reportesVolcanes/20170307102709928RAV_Araucania_Febrero_2017_N%C2%B002.pdf. Accessed 17 Apr 2022

SERNAGEOMIN (2020) Ranking de riesgo específico de volcanes activos de Chile 2019. Servicio Nacional de Geología y Minería (SERNAGEOMIN), Santiago, Chile. Available at: https://www.sernageomin.cl/wp-content/uploads/2020/07/2Ranking-2019_Tabla_Final.pdf. Accessed 28 Jan 2022

Shea T, Hammer JE (2013) Kinetics of cooling-and decompression-induced crystallization in hydrous mafic-intermediate magmas. J Volcanol Geotherm Res 260:127–145

Shreve T, Grandin R, Boichu M et al (2019) From prodigious volcanic degassing to caldera subsidence and quiescence at Ambrym (Vanuatu): the influence of regional tectonics. Sci Rep 9:18868. https://doi.org/10.1038/s41598-019-55141-7

Silva Parejas C, Druitt TH, Robin C et al (2010) The Holocene Pucón eruption of Volcán Villarrica, Chile: deposit architecture and eruption chronology. Bull Volcanol 72:677–692. https://doi.org/10.1007/s00445-010-0348-9

Sisson TW, Grove TL (1993) Temperatures and H2O contents of low-MgO high-alumina basalts. Contrib to Mineral Petrol 113(2):167–184. https://doi.org/10.1007/BF00283226

Spina L, Cannata A, Morgavi D, Perugini D (2019) Degassing behaviour at basaltic volcanoes: New insights from experimental investigations of different conduit geometry and magma viscosity. Earth Sci Rev 192:317–336

Sun SS, McDonough WF (1989) Chemical and isotopic systematics of oceanic basalts: implications for mantle composition and processes. Geol Soc Spec Publ 42(1):313–345

Tassara A, Götze HJ, Schmidt S, Hackney R (2006) Three-dimensional density model of the Nazca plate and the Andean continental margin. J Geophys Res: Solid Earth 111:B09404

Valade S, Lacanna G, Coppola D et al (2016) Tracking dynamics of magma migration in open-conduit systems. Bull Volcanol 78(11):1–12

Van Daele M, Moernaut J, Silversmit G et al (2014) The 600 yr eruptive history of Villarrica Volcano (Chile) revealed by annually laminated lake sediments. GSA Bull 126:481. https://doi.org/10.1130/B30798.1

Viccaro M, Cannata A, Cannavò F et al (2021) Shallow conduit dynamics fuel the unexpected paroxysms of Stromboli volcano during the summer 2019. Sci Rep 11(1):1–15

Waters LE, Lange RA (2015) An updated calibration of the plagioclase-liquid hygrometer-thermometer applicable to basalts through rhyolites. Am Mineral 100(10):2172–2184. https://doi.org/10.2138/am-2015-5232

Wardman J, Sword-Daniels V, Stewart C, Wilson T (2012) Impact assessment of the May 2010 eruption of Pacaya volcano, Guatemala. GNS Sci Rep 2012(09):90

Witham F, Woods AW, Gladstone C (2006) An analogue experimental model of depth fluctuations in lava lakes. Bull Volcanol 69(1):51–56

Witter JB, Kress VC, Delmelle P, Stix J (2004) Volatile degassing, petrology, and magma dynamics of the Villarrica Lava Lake, Southern Chile. J Volcanol Geotherm Res 134(4):303–337

Yamaguchi T, Ohzono H, Yamagami M et al (2010) Ion hydration in aqueous solutions of lithium chloride, nickel chloride, and caesium chloride in ambient to supercritical water. J Mol Liq 153(1):2–8

Zajacz Z, Halter W (2009) Copper transport by high temperature, sulfur-rich magmatic vapor: evidence from silicate melt and vapor inclusions in a basaltic andesite from the Villarrica volcano (Chile). Earth & Planet Sci Lett 282(1–4):115–121

Zellmer GF (2021) Gaining acuity on crystal terminology in volcanic rocks. Bull Volcanol 83(11):1–8

Zuccarello F, Schiavi F, Viccaro M (2021) Magma dehydration controls the energy of recent eruptions at Mt. Etna volcano. Terra Nova 33(4):423–429

Authors and Affiliations

Jorge E. Romero[1] · Eduardo Morgado[2] · Alessandro Pisello[3] · Felix Boschetty[4] · Maurizio Petrelli[3] · Francisco Cáceres[5] · Mohammad Ayaz Alam[6] · Margherita Polacci[1] · José L. Palma[7] · Fabio Arzilli[8] · Franco Vera[9] · Romina Gutiérrez[10] · Daniele Morgavi[11]

[1] Department of Earth and Environmental Sciences, University of Manchester, Manchester, UK

[2] Escuela de Geología, Universidad Mayor, Providencia, Santiago, Chile

[3] Department of Physics and Geology, University of Perugia, Perugia, Italy

[4] School of Earth and Environment, University of Leeds, Leeds, UK

[5] Department of Earth and Environmental Sciences, Ludwig-Maximilians-Universität München, Munich, Germany

[6] Carrera de Geología, Facultad de Ingeniería, Universidad Andres Bello, Santiago, Chile

[7] Departamento de Ciencias de La Tierra, Facultad de Ciencias Químicas, Universidad de Concepción, Concepción, Chile

[8] School of Science and Technology, Geology Division, University of Camerino, Camerino, Italy

[9] Red Nacional de Vigilancia Volcánica, Servicio Nacional de Geología y Minería, Santiago, Chile

[10] Departamento de Geología, Universidad de Chile, Santiago, Chile

[11] Dipartimento Di Scienze Della Terra, Dell'Ambiente E Delle Risorse (DiSTAR), Universita` Degli Studi Di Napoli Federico II, Naples, Italy